

# Stochastic neuropeptide signals compete to calibrate the rate of satiation

<https://doi.org/10.1038/s41586-024-08164-8>

Received: 19 July 2023

Accepted: 7 October 2024

Published online: 6 November 2024

 Check for updates

Stephen X. Zhang<sup>1,7</sup>, Angela Kim<sup>1,7</sup>, Joseph C. Madara<sup>1</sup>, Paula K. Zhu<sup>1</sup>, Lauren F. Christenson<sup>1</sup>, Andrew Lutas<sup>1,5</sup>, Peter N. Kalugin<sup>1</sup>, Praneel S. Sunkavalli<sup>1</sup>, Yihan Jin<sup>2,3,6</sup>, Akash Pal<sup>2,6</sup>, Lin Tian<sup>2,6</sup>, Bradford B. Lowell<sup>1</sup> & Mark L. Andermann<sup>1,4</sup>

Neuropeptides have important roles in neural plasticity, spiking and behaviour<sup>1</sup>. Yet, many fundamental questions remain regarding their spatiotemporal transmission, integration and functions in the awake brain. Here we examined how MC4R-expressing neurons in the paraventricular nucleus of the hypothalamus (PVH<sup>MC4R</sup>) integrate neuropeptide signals to modulate feeding-related fast synaptic transmission and titrate the transition to satiety<sup>2–6</sup>. We show that hunger-promoting AgRP axons release the neuropeptide NPY to decrease the second messenger cAMP in PVH<sup>MC4R</sup> neurons, while satiety-promoting POMC axons release the neuropeptide  $\alpha$ MSH to increase cAMP. Each release event is all-or-none, stochastic and can impact multiple neurons within an approximately 100- $\mu$ m-diameter region. After release, NPY and  $\alpha$ MSH peptides compete to control cAMP—the amplitude and persistence of NPY signalling is blunted by high  $\alpha$ MSH in the fed state, while  $\alpha$ MSH signalling is blunted by high NPY in the fasted state. Feeding resolves this competition by simultaneously elevating  $\alpha$ MSH release and suppressing NPY release<sup>7,8</sup>, thereby sustaining elevated cAMP in PVH<sup>MC4R</sup> neurons throughout a meal. In turn, elevated cAMP facilitates potentiation of feeding-related excitatory inputs with each bite to gradually promote satiation across many minutes. Our findings highlight biochemical modes of peptide signal integration and information accumulation to guide behavioural state transitions.

Arcuate hypothalamic neurons integrate hormonal, interoceptive and external cues, and use neuropeptides to regulate food intake, energy expenditure and body weight<sup>2,5–16</sup>. These peptides bind to G-protein-coupled receptors that signal by increasing<sup>17,18</sup> or decreasing<sup>19</sup> intracellular cAMP concentration. Mutations in these receptor-to-cAMP cascades are associated with obesity<sup>20</sup>. One important target of these peptides is the satiety-promoting PVH<sup>MC4R</sup> neurons<sup>2–5,21,22</sup>. How these hunger and satiety peptides are integrated at the level of cAMP, and how cAMP, in turn, controls spiking of PVH<sup>MC4R</sup> neurons remain largely unclear. One major obstacle has been the inability to directly monitor cAMP levels in individual PVH<sup>MC4R</sup> neurons in vivo, because cAMP dynamics are invisible using conventional electrophysiological or calcium recordings. To overcome these technical challenges, we assembled a suite of tools to stimulate and track endogenous neuropeptide release from AgRP and POMC neurons, and to measure and manipulate cAMP levels in individual PVH<sup>MC4R</sup> neurons, in awake mice across seconds to hours<sup>23</sup>.

Neuropeptides are found in dense-core vesicles that sparsely populate chemical synapses<sup>1,24</sup>. Once released, they could potentially diffuse across long distances before driving signalling in downstream neurons<sup>1,25–28</sup>. However, many questions regarding this process remain, particularly in the awake brain, including questions of how frequently

the neuropeptides are released, and how they travel; the timescales and state-dependence of peptidergic effects on downstream neurons; whether multiple neuropeptides act on the same intracellular signals; and how changes in intracellular signalling impact neural activity and behaviour. Here we investigate the integration and competition of peptide-evoked biochemical signals in awake mice and ultimately describe how this biochemical computation leads to gradual changes in synaptic strength and feeding behaviour (Fig. 1a).

## Reducing cAMP signalling causes obesity

Previous biochemical characterizations of feeding-related neuropeptide receptors show converging signalling through cAMP<sup>5,17,19,29</sup> (Fig. 1a). However, knocking out the relevant G proteins in PVH<sup>MC4R</sup> neurons from birth has mixed effects on feeding<sup>30,31</sup>, and alternative signalling mechanisms have been suggested<sup>5,32–34</sup>. To acutely and selectively reduce cAMP, we expressed a constitutively active phosphodiesterase (PDE), PDE4D3-Cat<sup>23</sup>, in PVH<sup>MC4R</sup> neurons in adult mice (Fig. 1b; tool validation is shown in Extended Data Fig. 1a). Injection of AAV expressing PDE4D3-Cat nearly doubled mouse body weight and fat-mass percentage within 4 weeks (Fig. 1c,d, Extended Data Fig. 1b,c and Supplementary Table 1). These obesity phenotypes can be explained by

<sup>1</sup>Division of Endocrinology, Diabetes and Metabolism, Beth Israel Deaconess Medical Center, Harvard Medical School, Boston, MA, USA. <sup>2</sup>Department of Biochemistry and Molecular Medicine, School of Medicine, University of California, Davis, Sacramento, CA, USA. <sup>3</sup>Neuroscience Graduate Group, Center for Neuroscience, University of California, Davis, Sacramento, CA, USA.

<sup>4</sup>Department of Neurobiology, Harvard Medical School, Boston, MA, USA. <sup>5</sup>Present address: Diabetes, Endocrinology and Obesity Branch, National Institute of Diabetes and Digestive and Kidney Diseases, National Institutes of Health, Bethesda, MD, USA. <sup>6</sup>Present address: Max Planck Florida Institute for Neuroscience, One Max Planck Way, Jupiter, FL, USA. <sup>7</sup>These authors contributed equally: Stephen X. Zhang, Angela Kim. <sup>✉</sup>e-mail: [x.stephen.zhang@gmail.com](mailto:x.stephen.zhang@gmail.com); [manderma@bidmc.harvard.edu](mailto:manderma@bidmc.harvard.edu)

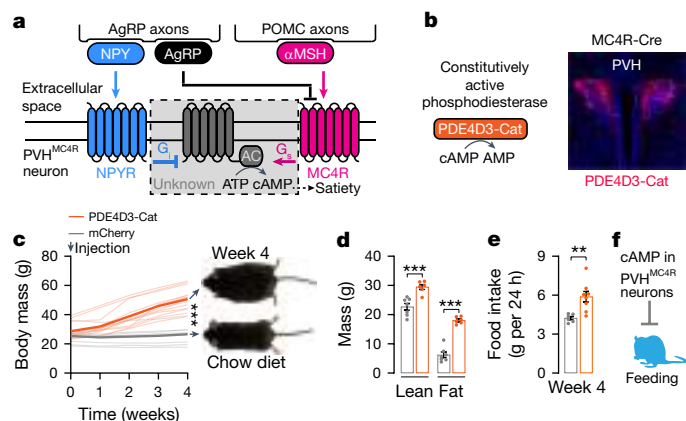


**Fig. 1 | Accelerating cAMP degradation in PVH<sup>MC4R</sup> neurons causes obesity.** **a**, Model of bidirectional regulation of cAMP by hunger and satiety peptides. AC, adenylyl cyclase; G<sub>i</sub>, inhibitory G protein; G<sub>s</sub>, stimulatory G protein. **b–e**, AAV expression of PDE4D3-Cat in PVH<sup>MC4R</sup> neurons (**b**) resulting in significant weight gain (**c**;  $n = 9–15$  mice), elevated lean and fat mass (**d**;  $n = 6–7$ ) and hyperphagia (**e**;  $n = 6–8$ ). **f**, cAMP signalling in PVH<sup>MC4R</sup> neurons is important for reducing feeding. For **d** and **e**, data are mean  $\pm$  s.e.m. across mice. Statistical analysis was performed using unpaired *t*-tests (**c**) and one-way analysis of variance (ANOVA) (**d** and **e**). NS, not significant. \* $P < 0.05$ , \*\* $P < 0.01$ , \*\*\* $P < 0.001$ . Statistical details and sex-specific characterizations are provided in Supplementary Table 1.

hyperphagia (that is, overeating) (Fig. 1e and Extended Data Fig. 1d) but not decreased energy expenditure or impaired PVH<sup>MC4R</sup> neuron health (Extended Data Fig. 1e–u). Together with previous studies of PVH<sup>MC4R</sup> neurons<sup>4,21,22</sup>, these results show that cAMP signalling in PVH<sup>MC4R</sup> neurons is critical for suppressing feeding (Fig. 1f).

### Stochastic, state-dependent cAMP signals

αMSH released from satiety-promoting POMC neurons has been proposed to activate MC4R receptors, in turn elevating cAMP production in PVH<sup>MC4R</sup> neurons<sup>2,3,5,6,12,17,29</sup> (Fig. 2a). However, direct *in vivo* observation of endogenous peptide-induced changes in cAMP in these neurons is lacking. To assess the spatiotemporal dynamics of peptide transmission, we performed two-photon imaging of a cAMP sensor, cADDiS, in individual PVH<sup>MC4R</sup> neurons in awake, head-fixed mice through a GRIN lens<sup>23,35</sup>, together with optogenetic stimulation of POMC axons in the PVH (Fig. 2a). In fasted mice, single-trial photostimulation trains (8 s, 30 Hz; Methods and Fig. 2b (red shading)) could trigger large increments in cAMP that persisted for tens of seconds, but these increments occurred on different trials for different somas (Fig. 2b,c). As single-trial amplitudes of cAMP increments were bimodally distributed (Fig. 2c (inset)), we used a fixed-window classifier (Methods) to label trials as hits (large increases in cAMP) or misses (no change). The proportion of hit trials, or the hit rate, did not monotonically decrease or increase over time (Extended Data Fig. 2a). Instead, the stochastic, fixed-probability cAMP increments in individual neurons were effectively modelled by the rolling of a six-sided die (the dice model; Fig. 2d,e and Extended Data Fig. 2a,b).

We compared cAMP responses to POMC axon stimulation in ad libitum fed (fed) and chronically fasted (fasted) states. Although the frequencies of cAMP transients did not differ between states (Fig. 2f and Extended Data Fig. 2a–c), cAMP increments were much more prolonged in the fed state (Fig. 2f and Extended Data Fig. 2d,e). This difference was evident regardless of whether we averaged across all of the trials (Extended Data Fig. 2d) or only hit trials (Fig. 2f). POMC-axon-evoked cAMP increments showed around 80% larger peak amplitudes (Fig. 2g) and longer durations in the fed state (>5 min versus around 100 s; Extended Data Fig. 2e). Accordingly,

persistence (calculated as the ratio of the mean cAMP response magnitudes from 80 to 100 s and from 20 to 40 s after stimulus onset) was fivefold greater in fed mice (Fig. 2h). Together, these results show state-dependent efficacy of second-messenger signalling that is triggered by POMC axon activation.

Although the above results are consistent with αMSH- and MC4R-mediated cAMP increments (Fig. 2a), they do not directly confirm the involvement of this peptide or receptor. We therefore tested whether intracerebroventricular (i.c.v.) pre-infusion of the MC4R antagonist SHU9119 affects POMC-stimulation-evoked cAMP increments (histology and infusion validation is shown in Extended Data Fig. 2f–i). When we pre-infused SHU9119 (1 nmol in 2  $\mu$ l) in fed mice, it blocked 62% of POMC-stimulation-induced cAMP increments (Fig. 2i and Extended Data Fig. 2j,k) and reduced the amplitudes of the remaining hits by 50% (Fig. 2j and Extended Data Fig. 2l–o), together reflecting an 81% reduction in peptide transmission (Methods). These effects were consistent across mice (Extended Data Fig. 2k–m) and across fields of view (Extended Data Fig. 2n–o). Taken together, these results support a model of peptidergic transmission in which activation of POMC axons triggers MC4R-dependent, stochastic and state-dependent cAMP increments in PVH<sup>MC4R</sup> neurons.

### NPY-induced stochastic cAMP decrements

Hunger-promoting AgRP neurons also project to the PVH, where they release the neuropeptides NPY and AgRP to suppress cAMP<sup>2,3,5,19,36,37</sup> (Fig. 2k). Photostimulation of AgRP axons (8 s, 30 Hz) evoked stochastic, all-or-none cAMP decrements in PVH<sup>MC4R</sup> somas (Fig. 2l). Similar to POMC-stimulation-evoked cAMP increments, the probability of an AgRP-evoked cAMP decrement was also well modelled by the dice model (Fig. 2n), and the hit rate was not strongly modulated by hunger state (Extended Data Fig. 3a). In hit trials, cAMP decrements also showed state dependence, as they were larger and more persistent in fasted mice (Fig. 2o–q and Extended Data Fig. 3b,c).

Out of all of the neuropeptides and small-molecule neurotransmitters that AgRP neurons release (such as GABA, AgRP, NPY), NPY mediates a significant proportion of the hunger-promoting effects, particularly those lasting many minutes<sup>36</sup>. We therefore pre-infused antagonists for two NPY receptors (10 nmol BIBP3226 for NPY1R and 10 nmol CGP71683 for NPY5R, 4  $\mu$ l total, i.c.v.) that are known to be important for mediating the hunger-promoting effects of NPY<sup>38</sup>. In fed mice, these antagonists blocked 71% of hits and reduced hit amplitudes by 66% in a consistent manner across all mice (Fig. 2r,s and Extended Data Fig. 3d–l). These findings show that NPY mediates around 90% of the acute influence of AgRP axons on cAMP signalling in PVH<sup>MC4R</sup> neurons, leaving a minor or redundant role for the co-transmission of the AgRP peptide<sup>36,39,40</sup> (Methods). Together, the above *in vivo* findings show that αMSH transmission from POMC axons and NPY transmission from AgRP axons mediate the majority of evoked increments and decrements in cAMP, respectively (Fig. 2t).

### Stochastic and local peptide release

The probabilistic nature of the neuropeptide-mediated cAMP signalling described above is redolent of stochastic neurotransmitter release, albeit with the major distinction that the probability of a cAMP transient is low despite bulk stimulation of many AgRP or POMC axons. To ascertain whether stochasticity in cAMP signalling reflects stochasticity in neuropeptide release, we expressed a fluorescent NPY sensor, npyLight1.0, in PVH neurons (Fig. 3a and Extended Data Fig. 4a). To induce endogenous NPY release, we photostimulated AgRP axons in the PVH in brain slices using trains of varying durations (15.5 Hz, 2 s, 4 s, 8 s, 16 s; Extended Data Fig. 4b–e). AgRP axon photostimulation triggered npyLight1.0 transients stochastically (Fig. 3b and Extended Data Fig. 4b–g), and the amplitude of hits remained consistent for





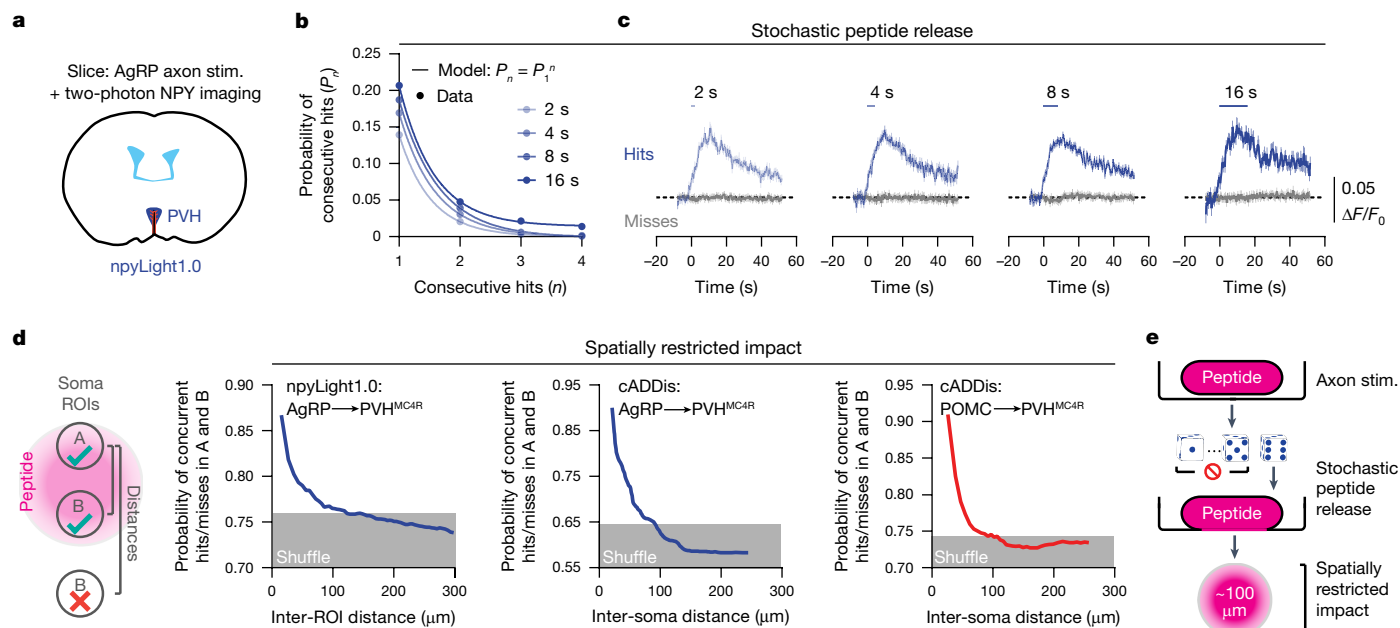


**Fig. 3 | A stochastic and spatially restricted mode of neuropeptide release.**

**a**, Measurement of NPY release after AgRP axon stimulation in brain slices from fed mice using npyLight1.0. **b,c**, Increasing the duration of 15.5 Hz photostimulation from 2 s to 16 s only modestly elevated hit rates of npyLight transients from 14% to 21% (**b**;  $n = 16,439$ – $19,969$  trials, 7 mice). Hit amplitudes remained unchanged (**c**; from left to right,  $n = 2,632$ ,  $2,782$ ,  $3,736$  and  $3,595$  hits). **d**, The probability of concurrent hits or concurrent misses in two somas

decreases as the inter-soma distance increases. The distance beyond which the probability drops to chance levels is consistently around  $100\ \mu\text{m}$  for npyLight1.0 (left) and cADDIs (middle) recordings during AgRP axon stimulation, as well as for cADDIs recordings during POMC axon stimulation (right). ROIs, regions of interest. **e**, Stochastic release leads to temporally and spatially sparse neuropeptide signalling. Data are mean  $\pm$  s.e.m. across hits (**c**).

and for NPY signals measured at different locations (Fig. 3d). Taken together, these results support a spatiotemporally sparse mode of neuropeptide transmission in which stochastic neuropeptide-release events evoke local cAMP changes in compartments within and across PVH<sup>MC4R</sup> neurons (Fig. 3e).

## The peptide competition hypothesis

As hunger and satiety peptides are maximally efficacious in different states (Fig. 2), it is unlikely for such state dependence to stem from one common variable such as arousal level. We also confirmed that the state dependence is not due to changes in excitability of stimulated axons (Extended Data Fig. 5a,b) or cAMP clearance (Extended Data Fig. 5c). We therefore considered whether competing peptide actions on cAMP production could underlie this state dependence.

POMC neurons are known to exhibit elevated ongoing activity in the fed state<sup>7,8</sup>, which probably results in a tonic level of  $\alpha\text{MSH}$  release that could hinder NPY-induced cAMP decrements (Fig. 4a). To test this peptide competition hypothesis, we sought to artificially mimic this receptor competition by directly infusing  $1\ \text{nmol}$  of  $\alpha\text{MSH}$  into the brain ( $2\ \mu\text{l}$ , i.c.v.), which was sufficient to elevate cAMP in PVH<sup>MC4R</sup> neurons (Extended Data Fig. 2h,i). In the fasted state, this manipulation did not affect the hit rate of AgRP stimulation-induced cAMP decrements (Extended Data Fig. 6a–c) but did cause a significant decrease in the amplitude (78%) and persistence (86%) of decrements across all mice and fields of view (Fig. 4b and Extended Data Fig. 6d,e). When we replaced the i.c.v. pre-infusion of  $1\ \text{nmol}$  of  $\alpha\text{MSH}$  with intraperitoneal (i.p.) delivery of the MC4R agonist, melanotan II (MTII), it also reduced the cAMP decrement amplitude by 46% and persistence by 41% (Extended Data Fig. 6f–k) in a manner similar to our observations in fed mice.

The peptide competition hypothesis also predicts that higher steady-state levels of NPY related to elevated AgRP neuron firing in the fasted state could activate NPY receptors and blunt  $\alpha\text{MSH}$ -induced

cAMP production<sup>7,8,14,41</sup> (Fig. 4c). We therefore tested whether NPY delivery ( $0.5\ \text{nmol}$  in  $1\ \mu\text{l}$ , i.c.v.) would weaken POMC-stimulation-evoked cAMP increments in fed mice (Fig. 4c). Pre-infusion of NPY in fed mice (Extended Data Fig. 3e,f) reduced the cAMP increment amplitude by 54% and persistence by 83% (Fig. 4d and Extended Data Fig. 6l–p) in a manner similar to that observed in fasted mice. While an MC4R

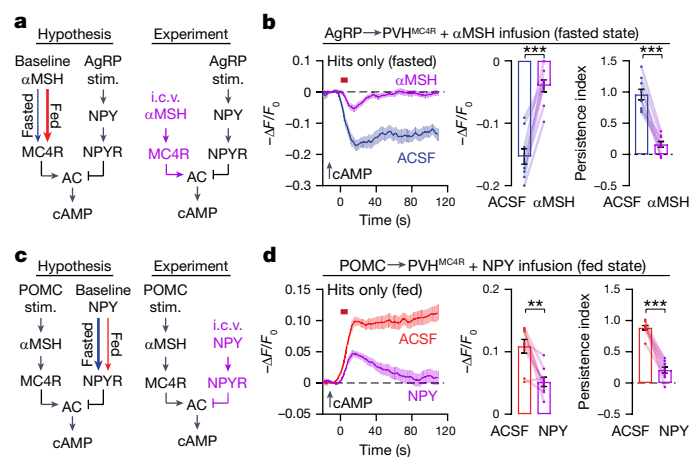


**Fig. 4 | Neuropeptide competition underlies state-dependent cAMP signalling.**

**a**, When endogenously elevated in fed mice or experimentally elevated in fasted mice, basal  $\alpha\text{MSH}$  levels should curb AgRP axon stimulation-induced cAMP decrements. **b**, In fasted mice,  $\alpha\text{MSH}$  pre-infusion ( $1\ \text{nmol}$ , i.c.v.) reduced the hit amplitude and persistence of cAMP decrements.  $n = 129$ – $145$  hits from 9 FOVs and 3 mice. **c**, Increased basal NPY levels should curb POMC axon stimulation-induced cAMP increments. **d**, In fed mice, NPY pre-infusion ( $0.5\ \text{nmol}$ , i.c.v.) reduced the hit amplitude and persistence of cAMP increments.  $n = 234$ – $291$  hits from 9 FOVs and 3 mice. For **b** and **d**, data are mean  $\pm$  s.e.m. across hits (traces) and FOVs (bar graphs); statistical analysis was performed using paired  $t$ -tests.

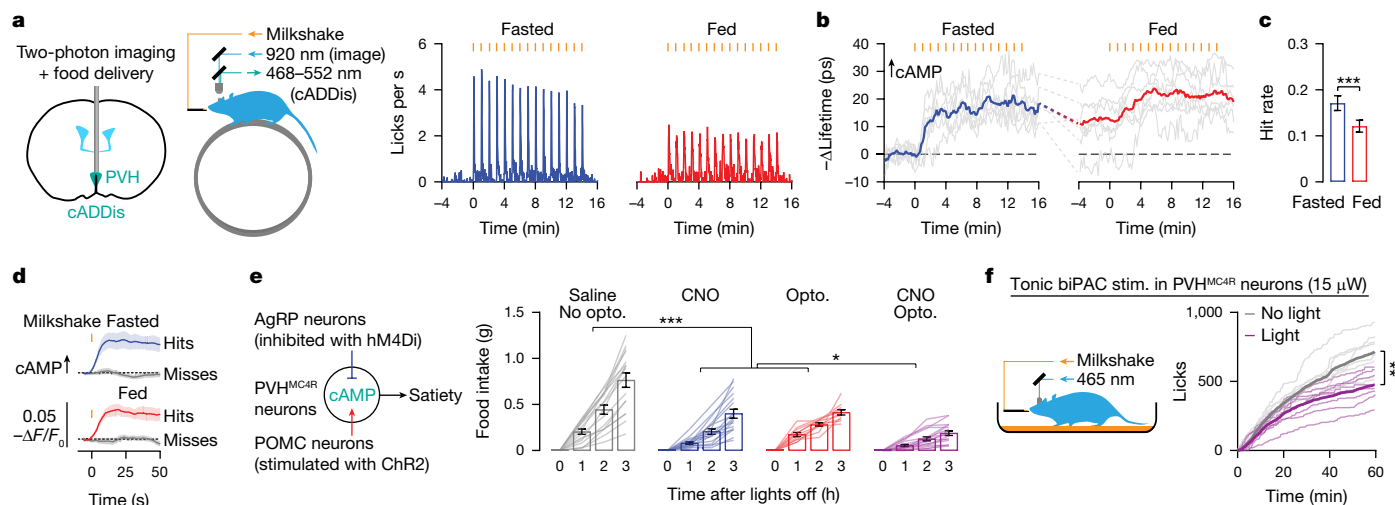


**Fig. 5 | Stochastic and persistent cAMP increments during feeding set the rate of satiation.** **a**, Periodic milkshake delivery to head-fixed mice resulted in transient and time-locked increases in lick rate that were reliably observed under the fasted and fed conditions.  $n = 6$  mice. **b**, cAMP in PVH<sup>MC4R</sup> neurons climbed to a steady-state level within around four 1 min trials in both conditions, albeit from a higher initial level in the fed state. The grey traces show the mean soma cADDis lifetime changes per FOV. The blue and red traces show the mean across 7–11 FOVs and 6 mice. **c, d**, Feeding-induced cAMP transients were stochastic in both fasted and fed states (**c** shows hit rates and **d** shows cAMP traces).  $n = 2,103$  fasted trials and 2,405 fed trials. **e**, Either chemogenetic

inhibition of AgRP neurons (hM4Di, i.p. clozapine *N*-oxide (CNO)) or optogenetic stimulation of POMC axons in the PVH (ChR2) suppressed dark-phase feeding in freely moving mice, but the suppression was strongest when the two manipulations were combined ( $n = 11$ –17 mice), consistent with decreased peptide competition. **f**, Continuous photostimulation of cAMP production (biPAC,  $\sim 15 \mu\text{W}$ ) in PVH<sup>MC4R</sup> neurons reduced the cumulative lick rate in fasted mice.  $n = 8$  mice. Data area mean  $\pm$  95% confidence intervals of hit rates (**c**); and mean  $\pm$  s.e.m. across hits (**d**) and mice (**e**). Statistical analysis was performed using one-way ANOVA (**e**) and paired *t*-tests (**f**).

antagonist also reduced the cAMP increment amplitude, it did not attenuate the persistence (Fig. 2j), demonstrating that merely blocking POMC-evoked signalling at MC4Rs without introducing downstream competition at the level of cAMP is not sufficient to fully mimic state-dependent modulation.

The extent to which  $\alpha\text{MSH}$  and NPY could curb each other's cAMP signal should depend on their relative concentrations. To test this idea, we identified rare cases in which the same PVH<sup>MC4R</sup> neuron exhibited cAMP transients on two consecutive trials (probably due to two sequential peptide-release events in the same spatial vicinity; Extended Data Fig. 6q). As predicted, cAMP decrements or increments were larger and more persistent on the second hit as compared to the first hit during AgRP or POMC neuron stimulation, respectively (Extended Data Fig. 6q,r). Likewise, concentrating the stimulation of peptide release in time by shortening the inter-stimulus interval (from 52 s to 2 s) triggered cAMP increments and decrements that lasted more than 10 min (ref. 36) (Extended Data Fig. 6s,t). Together, these results show that neuropeptide competition is dose dependent.

## Stochastic cAMP signalling during feeding

Competition between  $\alpha\text{MSH}$  and NPY signalling could provide a means to filter out co-excitation or co-inhibition of AgRP and POMC neurons while promoting stronger modifications of cAMP levels during opposing shifts in the activity of the two neuronal populations. Such opposite-direction modulation of AgRP and POMC neuron activity has been observed for almost all regulators of energy balance (leptin<sup>42</sup>, ghrelin<sup>7,43</sup>, feeding<sup>7,8</sup>, exercise<sup>44</sup>) (Extended Data Fig. 7a,b). To experimentally characterize cAMP dynamics during natural feeding, we designed a feeding task in which drops of milkshake (Ensure; 15  $\mu\text{l}$  per trial) were delivered to a head-fixed mouse with the same 60 s intertrial interval as above (Fig. 5a). Two-photon fluorescence lifetime imaging microscopy (2p-FLIM) measurements of absolute cAMP levels showed that, in both fasted and fed states, the average cAMP level of PVH<sup>MC4R</sup> neurons gradually rose in the first  $\sim 4$  trials and plateaued for the remainder of the session while the mice were still feeding (Fig. 5b

and Extended Data Fig. 7c). Even before food consumption, cAMP levels in the fed state were higher than in the fasted state (Fig. 5b), consistent with elevated baseline extracellular levels of satiety peptides. We found that feeding-evoked cAMP transients were also stochastic (Fig. 5c,d and Extended Data Fig. 7d–i). These results demonstrate a steady-state elevation in cAMP levels as a result of accruing stochastic cAMP transients in PVH<sup>MC4R</sup> neurons.

To examine whether the simultaneous drop in AgRP neuron activity and rise in POMC neuron activity during feeding is important for regulating food intake, we bred *Pomc-dre; AgRP-cre* mice and independently stimulated POMC neurons (with Dre-dependent ChR2) and inhibited AgRP neurons (with Cre-dependent hM4Di) (Fig. 5e). Either manipulation alone reduced feeding, but the combination of the two led to greater feeding suppression in a multiplicative manner<sup>10,45,46</sup> (Fig. 5e and Extended Data Fig. 7j–l). Thus, peptide competition at the level of cAMP production may function as a biochemical filter that favours opposite-direction changes in the levels of hunger and satiety peptides.

If the observed cAMP elevation during feeding is important for satiety, additional elevation of cAMP in PVH<sup>MC4R</sup> neurons should further reduce food intake. As an initial test, we used biPAC (a light-activated adenylyl cyclase) to bypass neuropeptide signalling and directly stimulate cAMP production in PVH<sup>MC4R</sup> neurons. We found that a tonic, low level of biPAC activation reduced feeding in both freely moving and head-fixed refeeding paradigms involving ad libitum access to milkshake through a lickspout (Fig. 5f and Extended Data Fig. 8a–c). Using a cue-based feeding assay, we found that phasic biPAC stimulation on each trial did not acutely suppress feeding, but gradually accelerated the onset of persistent satiety in a dose-dependent manner (details are provided in Extended Data Fig. 8d–o).

## cAMP potentiates feeding-related inputs

How cAMP in PVH<sup>MC4R</sup> neurons regulates feeding ultimately depends on how this second messenger alters the activity of these satiety-promoting neurons. A previous study found that prolonged incubation with  $\alpha\text{MSH}$  in brain slices strengthens excitatory inputs to PVH<sup>MC4R</sup> neurons<sup>47</sup>, but

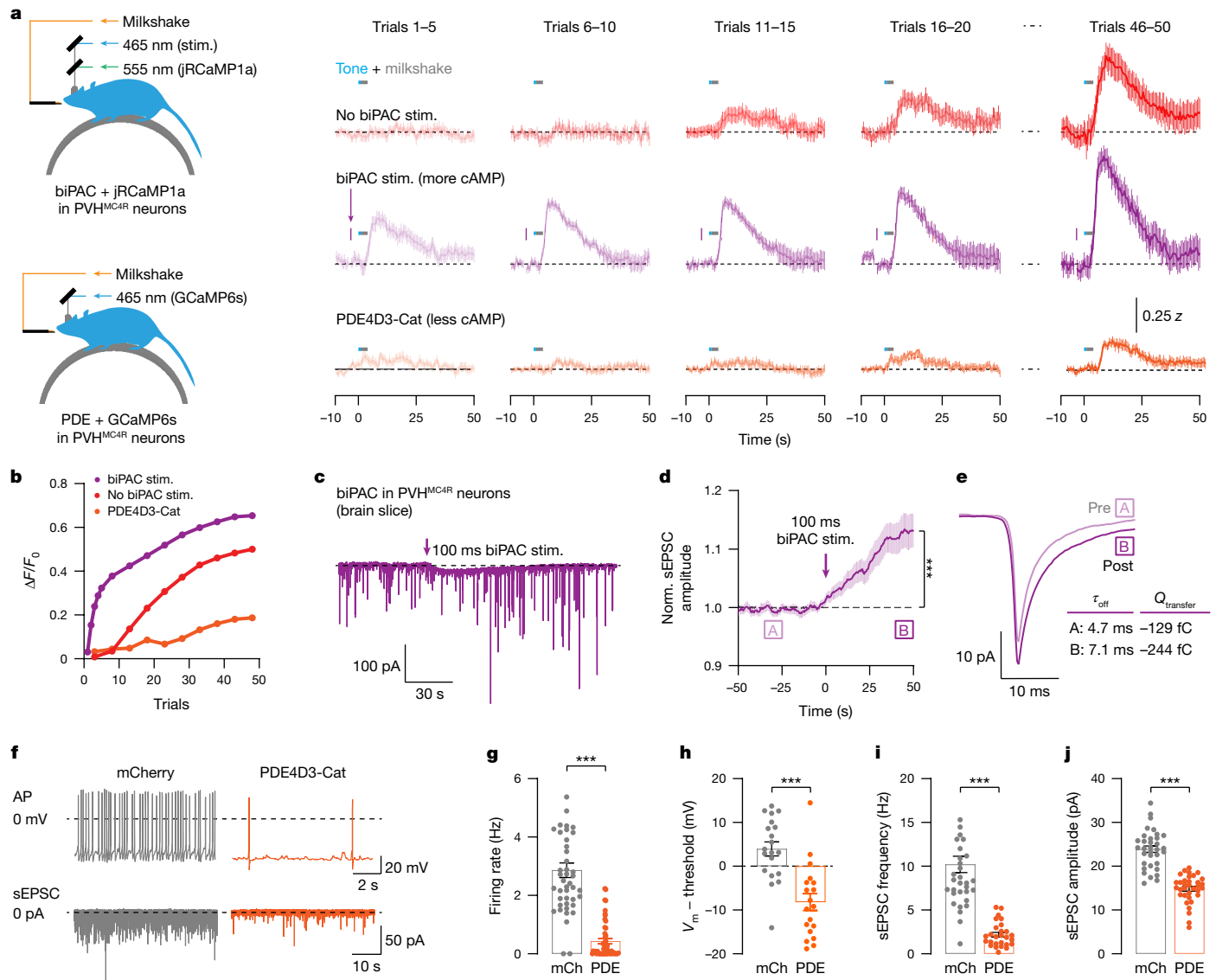


**Fig. 6 | cAMP potentiates feeding-related excitatory input to PVH<sup>MC4R</sup> neurons.** **a, b,** In a cued feeding assay in which fasted mice licked during a tone to obtain a small bolus of milkshake (1 trial per min), feeding-related jRCaMP1a calcium responses in PVH<sup>MC4R</sup> neurons grew across trials (red). Photostimulating biPAC (1 s) at 5 s before the cue accelerated the growth of responses (purple), while co-expressing PDE4D3-Cat blunted the growth (orange). **a,** Schematic. **b,** Single-trial mean responses (5–8 s after cue onset).  $n = 8$  mice per condition. **c–e,** Brief biPAC stimulation (100 ms; example in **c**) potentiated the amplitude of spontaneous excitatory inputs (**d**), thereby

sensitizing PVH<sup>MC4R</sup> neurons to excitatory inputs (**e**).  $n = 26$  cells, 5 fed mice. Norm., normalized. **f–h,** In PVH<sup>MC4R</sup> neurons in brain slices from fed mice, cAMP degradation by PDE4D3-Cat (**f**) reduced the firing rate (**g**), probably due to hyperpolarizing the membrane potential from supra- to sub-threshold (**h**).  $n = 44–50$  cells and 10 mice (**g**), and  $n = 19–20$  cells and 6 mice (**h**). mCh, mCherry control. **i, j,** PDE4D3-Cat expression reduced spontaneous EPSC frequency (**i**) and EPSC amplitude (**j**) in PVH<sup>MC4R</sup> neurons.  $n = 27–34$  cells from 10 mice each. Data are mean  $\pm$  s.e.m. across mice (**a**) and cells (**d** and **g–j**). For **g–j**, statistical analysis was performed using unpaired *t*-tests.

did not determine the involvement of cAMP or the dynamics of the synaptic plasticity *in vivo* during feeding.

We used jRCaMP1a fibre photometry to record calcium transients in PVH<sup>MC4R</sup> neurons during a conditioned feeding task, in which fasted mice lick during an audible cue to obtain milkshake reward (1 trial per min). In contrast to the presence of cAMP responses in early trials (Extended Data Fig. 7f–i), calcium responses to food consumption were absent in the first five trials (Extended Data Fig. 9a), consistent with previous reports<sup>48</sup>. However, calcium responses gradually developed over the next 10 trials and became clearly visible after 50 trials (Fig. 6a (top), 6b and Extended Data Fig. 9a), at which point the mice had ingested around 1.5 ml of milkshake and were about 50% satiated. Calcium responses showed a delayed increase that peaked around 4 s after the licking onset (Fig. 6a (top) and Extended

Data Fig. 9a). PVH<sup>MC4R</sup> neurons were also more spontaneously active at the end of the session (Extended Data Fig. 9b). These gradual increases in food-consumption-evoked and ongoing activity in PVH<sup>MC4R</sup> neurons are consistent with the key role of PVH<sup>MC4R</sup> neuron activity in promoting satiety<sup>2,4,5,12,21,22,47</sup>.

To test the potential involvement of cAMP in regulating the development of calcium responses, we artificially drove cAMP production in these same PVH<sup>MC4R</sup> neurons through brief biPAC photostimulation 5 s before each cue. Although the temporal profile of each PVH<sup>MC4R</sup> response to food consumption did not change, responses emerged as early as within the first five trials—a time when control traces were flat (Fig. 6a (top and middle), 6b and Extended Data Fig. 9c). These feeding-related calcium responses during biPAC-stimulation sessions continued to grow across trials, ultimately exceeding the amplitude

of control traces (Fig. 6a (top and middle) and 6b). In the absence of feeding, biPAC stimulation did not excite PVH<sup>MC4R</sup> neurons in vivo<sup>49,50</sup> (Fig. 6a and Extended Data Fig. 9d–g). The accelerated emergence of excitation is probably caused by cAMP-mediated synaptic plasticity that strengthens excitatory inputs<sup>47,51</sup>, as whole-cell recordings showed that biPAC-evoked cAMP production triggers an approximately 13% potentiation of spontaneous excitatory postsynaptic current (sEPSC) amplitudes and an 89% increase in charge transfer (Fig. 6c–e; additional brain slice data are shown in Extended Data Fig. 9h–j and Supplementary Table 2).

When we selectively blocked cAMP signalling in PVH<sup>MC4R</sup> neurons with PDE4D3-Cat, feeding-related calcium responses emerged substantially later within the session and were weaker even in the final trials (Fig. 6a,b). Whole-cell recordings in brain slices from fed mice showed that PDE4D3-Cat expression decreased the spontaneous firing rate of PVH<sup>MC4R</sup> neurons (Fig. 6f,g and Extended Data Fig. 9k) by hyperpolarizing the membrane potential from mostly supra-threshold to 8.1 mV below threshold (Fig. 6h and Extended Data Fig. 9l,m). This PDE4D3-Cat-induced hyperpolarization can be explained by a 79% reduction in frequency and a 38% reduction in amplitude of sEPSCs (Fig. 6i,j and Extended Data Fig. 9n–o). No changes in the neurons' passive properties were observed (Extended Data Fig. 9p–r). These characterizations support a model in which PDE4D3-Cat expression weakens excitatory synaptic drive to PVH<sup>MC4R</sup> neurons<sup>47</sup>, thereby hyperpolarizing these neurons sufficiently to diminish firing and ultimately promote hyperphagia as well as obesity (Fig. 1).

## Discussion

Our findings describe the biochemical mechanisms through which neuropeptidergic signals are integrated in space and in time to gradually calibrate neuronal plasticity and guide a measured transition from hunger to satiety (Extended Data Fig. 10). Below and in the Supplementary Discussion, we discuss the implications of these findings for understanding stochastic transmission, neuropeptide signal competition, interactions between fast and slow signals, and local volume transmission.

### Stochastic neuropeptide signalling

We show that neuropeptide-release events are intrinsically stochastic in in vivo and brain slice experiments (Figs. 2 and 3). Photostimulating AgRP axons triggered bimodally distributed NPY release (Extended Data Fig. 4b–e) and cAMP decrements in PVH<sup>MC4R</sup> neurons (Fig. 2m). The amount of local NPY release (that is, the size of npyLight1.0 transients) was insensitive to stimulation duration (Fig. 3c). Similarly, photostimulating POMC axons triggered bimodally distributed cAMP increments (Fig. 2c). We propose that each cAMP event reflects the exocytosis of a single dense-core vesicle<sup>1</sup>. Such stochasticity may be a consequence of the small number of dense-core vesicles in AgRP and POMC axonal boutons<sup>24</sup>.

Neuropeptides are replenished through axonal transport of dense-core vesicles at a rate of around  $1 \mu\text{m s}^{-1}$  (ref. 52)—faster than typical axonal transport but perhaps still insufficient to enable frequent dense-core vesicle release. In addition to preventing neuropeptide depletion, the sparsity of  $\alpha\text{MSH}$  and NPY release, together with their intrinsically persistent impact on cAMP, enables a calibrated form of information accumulation during repeated food consumption events and associated changes in AgRP and POMC neuron activity. During feeding, the rapid changes in firing of AgRP and POMC neurons scale with the amount of additional calories gained by imminent feeding behaviours<sup>2,7,8</sup>. We speculate that the gradual accumulation of peptide signalling can integrate this estimate of ingested calories during each bite to properly calibrate the strengthening of excitatory inputs to PVH<sup>MC4R</sup> neurons. This surprisingly slow mode of information integration through minutes-long biochemical signalling—after even a single

taste of food—may underlie the effectiveness of slow meal consumption in achieving earlier meal termination and reduced weight gain<sup>53</sup>.

### Peptide competition and energy balance

We hypothesize that the degree of elevation in cAMP determines the rate of satiation. If we compare the satiation rate to the speed of a car,  $\alpha\text{MSH}$  release from POMC axons and NPY release from AgRP axons may be analogous to the accelerator and brake pedals, respectively. Feeding simultaneously steps on the accelerator pedal (that is, increases POMC neuron activity and  $\alpha\text{MSH}$  release) and releases the brake (that is, inhibits AgRP neuron activity and NPY release). The resulting elevation in cAMP does not immediately drive a switch to a sated state, but instead increases the speed of approach towards satiety. This analogy also illustrates that the difference between the activity of POMC and AgRP neurons is particularly important for understanding when and how these inputs to PVH<sup>MC4R</sup> neurons will modify cAMP signalling. As such, concurrent increases or concurrent decreases in activity of AgRP and POMC neurons (for example, after cocaine, amphetamine or nicotine injection<sup>15</sup>) may not predict changes in feeding. Furthermore, knockout of either NPY<sup>54</sup> or an NPY receptor<sup>55</sup> has only a partial impact on ad libitum feeding, perhaps due to compensation through upregulated expression of a functionally similar peptide/peptide receptor or downregulation of the opponent peptide or receptor. Indeed, our findings show that cAMP signalling in PVH<sup>MC4R</sup> neurons is particularly sensitive to simultaneous opposite-direction changes in extracellular NPY and  $\alpha\text{MSH}$ , such as during feeding. Accordingly, MC4R agonists (such as setmelanotide<sup>56</sup>) may be more effective in promoting weight loss if used in combination with NPY antagonists or PDE inhibitors.

Hunger and satiety peptides inhibit each other's signalling efficacy (Fig. 4). At the molecular level, competition may take place through allosteric competition between  $G_{\text{as}}$ - and  $G_{\text{ai}}$ -binding sites on an adenylyl cyclase protein<sup>57</sup>. This mutual inhibition effectively mitigates the impact of fleeting changes in AgRP or POMC neuron activity (for example, when a mouse finds an unexpectedly inaccessible food source<sup>7</sup>) on the progression towards satiety. Such friction may be well suited for maintaining stable hunger and satiety states, in addition to other mechanisms hypothesized to carry out similar functions in this circuit<sup>58</sup>.

We inferred the presence and impact of baseline levels of peptides from experiments using agonists (Fig. 4b,d), repeated-hits analyses (Extended Data Fig. 6q,r), grouped-stimulation experiments (Extended Data Fig. 6s,t), state-dependent differences in basal cAMP (Fig. 5b) and previous in vivo recordings<sup>7,8,14</sup>. Owing to the amplifying effects of G protein signalling<sup>59</sup>, only a small fraction of peptide receptors may need to be activated to effectively blunt opposing peptide signalling. However, direct evidence for differences in the baseline levels and identity of various neuropeptides across fasted and fed states remains unclear. Given the slow diffusion of neuropeptides in the brain (around 10–20 s to spread  $100 \mu\text{m}$ )<sup>26</sup> and the presence of peptidases<sup>60</sup>, a substantial duration of tonic or experimentally evoked activity (for example, 98 s stimulation sequences in Extended Data Fig. 6s,t) in peptide-releasing neurons may be required for substantial extracellular accumulation of peptide. Shorter bursts of activity (2–16 s) may not achieve the same level of peptide accumulation (Fig. 3c). Future development of fluorescence-lifetime-compatible neuropeptide sensors will be instrumental in defining the state-dependent neuropeptidergic context surrounding each neuron, and how it affects signalling efficacy of a given neuropeptide.

### Online content

Any methods, additional references, Nature Portfolio reporting summaries, source data, extended data, supplementary information, acknowledgements, peer review information; details of author contributions and competing interests; and statements of data and code availability are available at <https://doi.org/10.1038/s41586-024-08164-8>.

1. van den Pol, A. N. Neuropeptide transmission in brain circuits. *Neuron* **76**, 98–115 (2012).
2. Andermann, M. L. & Lowell, B. B. Toward a wiring diagram understanding of appetite control. *Neuron* **95**, 757–778 (2017).
3. Cowley, M. A. et al. Integration of npy, agrp, and melanocortin signals in the hypothalamic paraventricular nucleus: evidence of a cellular basis for the adipostat. *Neuron* **24**, 155–163 (1999).
4. Garfield, A. S. et al. A neural basis for melanocortin-4 receptor-regulated appetite. *Nat. Neurosci.* **18**, 863–871 (2015).
5. Krashes, M. J., Lowell, B. B. & Garfield, A. S. Melanocortin-4 receptor-regulated energy homeostasis. *Nat. Neurosci.* **19**, 206–219 (2016).
6. Cone, R. D. Anatomy and regulation of the central melanocortin system. *Nat. Neurosci.* **8**, 571–578 (2005).
7. Chen, Y., Lin, Y.-C., Kuo, T.-W. & Knight, Z. A. Sensory detection of food rapidly modulates arcuate feeding circuits. *Cell* **160**, 829–841 (2015).
8. Mandelblat-Cerf, Y. et al. Arcuate hypothalamic AgRP and putative POMC neurons show opposite changes in spiking across multiple timescales. *eLife* **4**, e07122 (2015).
9. Deem, J. D., Faber, C. L. & Morton, G. J. AgRP neurons: regulators of feeding, energy expenditure, and behavior. *FEBS J.* **289**, 2362–2381 (2022).
10. Krashes, M. J. et al. Rapid, reversible activation of AgRP neurons drives feeding behavior in mice. *J. Clin. Invest.* **121**, 1424–1428 (2011).
11. Aponte, Y., Atasoy, D. & Sternson, S. M. AgRP neurons are sufficient to orchestrate feeding behavior rapidly and without training. *Nat. Neurosci.* **14**, 351–355 (2011).
12. Mercer, A. J., Hentges, S. T., Meshul, C. K. & Low, M. J. Unraveling the central proopiomelanocortin neural circuits. *Front. Neurosci.* **7**, 19 (2013).
13. Beutler, L. R. et al. Dynamics of gut-brain communication underlying hunger. *Neuron* **96**, 461–475 (2017).
14. Bettley, J. N. et al. Neurons for hunger and thirst transmit a negative-valence teaching signal. *Nature* **521**, 180–185 (2015).
15. Alhadeff, A. L. et al. Natural and drug rewards engage distinct pathways that converge on coordinated hypothalamic and reward circuits. *Neuron* **103**, 891–908 (2019).
16. Goldstein, N. et al. Hypothalamic detection of macronutrients via multiple gut-brain pathways. *Cell Metab.* **33**, 676–687 (2021).
17. Gantz, I. et al. Molecular cloning, expression, and gene localization of a fourth melanocortin receptor. *J. Biol. Chem.* **268**, 15174–15179 (1993).
18. Mountjoy, K. G., Robbins, L. S., Mortrud, M. T. & Cone, R. D. The cloning of a family of genes that encode the melanocortin receptors. *Science* **257**, 1248–1251 (1992).
19. Wahlestedt, C., Regunathan, S. & Reis, D. J. Identification of cultured cells selectively expressing Y1-, Y2-, or Y3-type receptors for neuropeptide Y/peptide YY. *Life Sci.* **50**, PL7–PL12 (1992).
20. Loos, R. J. F. & Yeo, G. S. H. The genetics of obesity: from discovery to biology. *Nat. Rev. Genet.* **23**, 120–133 (2022).
21. Balthasar, N. et al. Divergence of melanocortin pathways in the control of food intake and energy expenditure. *Cell* **123**, 493–505 (2005).
22. Shah, B. P. et al. MC4R-expressing glutamatergic neurons in the paraventricular hypothalamus regulate feeding and are synaptically connected to the parabrachial nucleus. *Proc. Natl Acad. Sci. USA* **111**, 13193–13198 (2014).
23. Zhang, S. X. et al. Hypothalamic dopamine neurons motivate mating through persistent cAMP signalling. *Nature* **597**, 245–249 (2021).
24. Atasoy, D. et al. A genetically specified connectomics approach applied to long-range feeding regulatory circuits. *Nat. Neurosci.* **17**, 1830–1839 (2014).
25. Jan, L. Y. & Jan, Y. N. Peptidergic synaptic transmission in sympathetic ganglia of the frog. *J. Physiol.* **327**, 219–246 (1982).
26. Xiong, H. et al. Probing neuropeptide volume transmission in vivo by simultaneous near-infrared light-triggered release and optical sensing. *Angew. Chem. Int. Ed.* **61**, e202206122 (2022).
27. Landgraf, R. & Neumann, I. D. Vasopressin and oxytocin release within the brain: a dynamic concept of multiple and variable modes of neuropeptide communication. *Front. Neuroendocrinol.* **25**, 150–176 (2004).
28. Qian, T. et al. A genetically encoded sensor measures temporal oxytocin release from different neuronal compartments. *Nat. Biotechnol.* <https://doi.org/10.1038/s41587-022-01561-2> (2023).
29. Mountjoy, K. G., Mortrud, M. T., Low, M. J., Simerly, R. B. & Cone, R. D. Localization of the melanocortin-4 receptor (MC4R) in neuroendocrine and autonomic control circuits in the brain. *Mol. Endocrinol.* **8**, 1298–1308 (1994).
30. Chen, M. et al. G $\alpha$  deficiency in the paraventricular nucleus of the hypothalamus partially contributes to obesity associated with G $\alpha$  mutations. *Endocrinology* **153**, 4256–4265 (2012).
31. Podyma, B. et al. The stimulatory G protein G $\alpha$  is required in melanocortin 4 receptor-expressing cells for normal energy balance, thermogenesis, and glucose metabolism. *J. Biol. Chem.* **293**, 10993–11005 (2018).
32. Ghamari-Langroudi, M. et al. G-protein-independent coupling of MC4R to Kir7.1 in hypothalamic neurons. *Nature* **520**, 94–98 (2015).
33. Lotta, L. A. et al. Human gain-of-function MC4R variants show signaling bias and protect against obesity. *Cell* **177**, 597–607 (2019).
34. Li, Y. Q. et al. G $\alpha_{11\alpha}$  and G $\alpha$  mediate distinct physiological responses to central melanocortins. *J. Clin. Invest.* **126**, 40–49 (2016).
35. Lutas, A., Fernando, K., Zhang, S. X., Sambangi, A. & Andermann, M. L. History-dependent dopamine release increases cAMP levels in most basal amygdala glutamatergic neurons to control learning. *Cell Rep.* **38**, 110297 (2022).
36. Chen, Y. et al. Sustained NPY signaling enables AgRP neurons to drive feeding. *eLife* **8**, e46348 (2019).
37. Bettley, J. N., Cao, Z. F. H., Ritola, K. D. & Sternson, S. M. Parallel, redundant circuit organization for homeostatic control of feeding behavior. *Cell* **155**, 1337–1350 (2013).
38. Nguyen, A. D. et al. Y1 and Y5 receptors are both required for the regulation of food intake and energy homeostasis in mice. *PLoS ONE* **7**, e40191 (2012).
39. Haskell-Luevano, C. & Monck, E. K. Agouti-related protein functions as an inverse agonist at a constitutively active brain melanocortin-4 receptor. *Regul. Pept.* **99**, 1–7 (2001).
40. Krashes, M. J., Shah, B. P., Koda, S. & Lowell, B. B. Rapid versus delayed stimulation of feeding by the endogenously released AgRP neuron mediators GABA, NPY, and AgRP. *Cell Metab.* **18**, 588–595 (2013).
41. Takahashi, K. A. & Cone, R. D. Fasting induces a large, leptin-dependent increase in the intrinsic action potential frequency of orexigenic arcuate nucleus neuropeptide Y/agouti-related protein neurons. *Endocrinology* **146**, 1043–1047 (2005).
42. Cowley, M. A. et al. Leptin activates anorexigenic POMC neurons through a neural network in the arcuate nucleus. *Nature* **411**, 480–484 (2001).
43. Chen, S.-R. et al. Ghrelin receptors mediate ghrelin-induced excitation of agouti-related protein/neuropeptide Y but not pro-opiomelanocortin neurons. *J. Neurochem.* **142**, 512–520 (2017).
44. He, Z. et al. Cellular and synaptic reorganization of arcuate NPY/AgRP and POMC neurons after exercise. *Mol. Metab.* **18**, 107–119 (2018).
45. De Solis, A. J. et al. Reciprocal activity of AgRP and POMC neurons governs coordinated control of feeding and metabolism. *Nat. Metab.* **6**, 473–493 (2024).
46. Biglari, N. et al. Functionally distinct POMC-expressing neuron subpopulations in hypothalamus revealed by intersectional targeting. *Nat. Neurosci.* **24**, 913–929 (2021).
47. Fenselau, H. et al. A rapidly acting glutamatergic ARC→PVH satiety circuit postsynaptically regulated by  $\alpha$ -MSH. *Nat. Neurosci.* **20**, 42–51 (2017).
48. Li, C. et al. Defined paraventricular hypothalamic populations exhibit differential responses to food contingent on caloric state. *Cell Metab.* **29**, 681–694 (2019).
49. Thorngquist, S. C., Pitsch, M. J., Auth, C. S. & Crickmore, M. A. Biochemical evidence accumulates across neurons to drive a network-level eruption. *Mol. Cell* **81**, 675–690 (2021).
50. Alvarado, J. S. et al. Transient cAMP production drives rapid and sustained spiking in brainstem parabrachial neurons to suppress feeding. *Neuron* **112**, 1416–1425 (2024).
51. Huganir, R. L. & Nicoll, R. A. AMPARs and synaptic plasticity: the last 25 years. *Neuron* **80**, 704–717 (2013).
52. Knabbe, J., Nassal, J. P., Verhage, M. & Kuner, T. Secretory vesicle trafficking in awake and anaesthetized mice: differential speeds in axons versus synapses. *J. Physiol.* **596**, 3759–3773 (2018).
53. Hawton, K. et al. Slow down: behavioural and physiological effects of reducing eating rate. *Nutrients* **11**, 50 (2018).
54. Hollpeter, G., Erickson, J. C., Seeley, R. J., Marsh, D. J. & Palmiter, R. D. Response of neuropeptide Y-deficient mice to feeding effectors. *Regul. Pept.* **75–76**, 383–389 (1998).
55. Marsh, D. J., Hollpeter, G., Kafer, K. E. & Palmiter, R. D. Role of the Y5 neuropeptide Y receptor in feeding and obesity. *Nat. Med.* **4**, 718–721 (1998).
56. Collet, T.-H. et al. Evaluation of a melanocortin-4 receptor (MC4R) agonist (setmelanotide) in MC4R deficiency. *Mol. Metab.* **6**, 1321–1329 (2017).
57. Sadana, R. & Dessauer, C. W. Physiological roles for G protein-regulated adenylyl cyclase isoforms: insights from knockout and overexpression studies. *Neurosignals* **17**, 5–22 (2009).
58. Yang, Y., Atasoy, D., Su, H. H. & Sternson, S. M. Hunger states switch a flip-flop memory circuit via a synaptic AMPK-dependent positive feedback loop. *Cell* **146**, 992–1003 (2011).
59. Spangler, S. M. & Bruchas, M. R. Optogenetic approaches for dissecting neuromodulation and GPCR signaling in neural circuits. *Curr. Opin. Pharmacol.* **32**, 56–70 (2017).
60. Turner, A. J., Matsas, R. & Kenny, A. J. Are there neuropeptide-specific peptidases? *Biochem. Pharmacol.* **34**, 1347–1356 (1985).

**Publisher's note** Springer Nature remains neutral with regard to jurisdictional claims in published maps and institutional affiliations.

Springer Nature or its licensor (e.g. a society or other partner) holds exclusive rights to this article under a publishing agreement with the author(s) or other rightsholder(s); author self-archiving of the accepted manuscript version of this article is solely governed by the terms of such publishing agreement and applicable law.

© The Author(s), under exclusive licence to Springer Nature Limited 2024



## Methods

### Data reporting

No statistical methods were used to predetermine sample size. Sample sizes were chosen to reliably measure experimental parameters and keep with standards of the relevant fields<sup>11,23,36,40,47,61–64</sup>, while remaining in compliance with ethical guidelines to minimize the number of experimental animals. Experiments did not involve experimenter-blinding, but randomization was used to determine experimental order and group assignments.

### Animals

All animal care and experimental procedures were approved by the Institutional Animal Care and Use Committee at Beth Israel Deaconess Medical Center (BIDMC). Animals were housed under a 12 h–12 h light–dark environment with standard mouse chow and water provided ad libitum, unless specified otherwise. Male and female mice older than 8 weeks were used in experiments, and the numbers of male and female mice were balanced to the degree allowed by each litter (Supplementary Table 1). Sex-specific analyses show consistent effects in males and females, but male mice were typically larger in size and ate more (Supplementary Table 1). We used the following genotypes: *B6.FVB-Tg(Pomc-cre)1Lowl/J (Pomc-cre*<sup>65</sup>, 010714, The Jackson Laboratory), *Pomc-dre*<sup>46</sup>, *Agrp*<sup>tm1(cre)Lowl/J (Agrp-IRES-cre<sup>66</sup>, 012899, The Jackson Laboratory), *Mc4r*<sup>tm3.1(cre)Lowl/J (MC4R-2A-Cre<sup>4</sup>, 030759, The Jackson Laboratory) and their F<sub>1</sub> progeny. We did not intentionally backcross mice to isogenize the backgrounds, but most mice were in the C57BL/6J background. Mice with implants (such as fibre, GRIN lens) were single-housed to avoid damage, and all other mice were group-housed.</sup></sup>

### Surgeries

Viral injections, fibre implantations and GRIN lens implantations were generally performed as described previously<sup>23</sup> with the following specifications. For experiments using a 400- $\mu$ m-diameter fibre or 500- $\mu$ m-diameter GRIN lens, to ensure a snug fit for the fibre or lens, to reduce brain motion and to accelerate recovery, we pre-set the insertion tracks by lowering needles with matching diameters (27 gauge or 25 gauge, respectively) to a depth of 0.1 mm above the final depth of the fibre or lens. For 22XX-gauge (MicroGroup, two Xs in the manufacture specifications) cannula implants, the track was set using a 22-gauge needle. In the initial experiments, GRIN lens placements were around 0.2 mm more lateral due to concerns about the potential impact on animal health, and the coordinates became the values below (which enabled better views of the PVH) once the initial health concerns were found to be unsubstantiated. All AAVs were injected at a titre of  $3\text{--}15 \times 10^{13}$  genome copies per ml (the volumes used are shown below). In experiments in which unmixed cADDis and PDE4D3-Cat viruses were used, both AAVs were pre-diluted 1:3 to a final titre of  $3\text{--}4 \times 10^{13}$  genome copies per ml before injections to minimize potential effects on cell health (which we verified in post hoc histological analyses). In the minority of cases in which viral expression was absent (<10% of surgeries), we excluded the data from subsequent analyses. All of the animals were allowed to recover for at least 3 weeks before the onset of experiments. No obvious capsid competition was seen in histology. Experiment-specific descriptions of surgical procedures are provided in Supplementary Methods.

### Pharmacological agents

NPY<sup>67–69</sup> (Tocris, 1153, 27A) was dissolved in ACSF (Tocris, 3525, 81A) at 500 pmol  $\mu$ l<sup>-1</sup> for i.c.v. experiments (500 pmol per mouse) and dissolved in water at 200 nM for slice experiments (200 nM).  $\alpha$ MSH<sup>70</sup> (Tocris, 2584, 6A) was dissolved in ACSF at 0.5 nmol  $\mu$ l<sup>-1</sup> and used for i.c.v. infusions (1 nmol per mouse). MTII (MC3R/MC4R agonist, Tocris, 25661, 6A) was dissolved in saline at 0.5  $\mu$ g  $\mu$ l<sup>-1</sup> and used for i.p. injections

(3 mg per kg). SHU9119<sup>71</sup> (MC3R/MC4R antagonist, Tocris, 3420, 6A) was dissolved in ACSF at 0.5 nmol  $\mu$ l<sup>-1</sup> and used for i.c.v. infusions (1 nmol per mouse). SHU9119 also blocks MC3R signalling<sup>71</sup>. However, to our knowledge,  $\alpha$ MSH is the only neuropeptide released from POMC neurons that binds to MC4R at high affinity<sup>72,73</sup>, and therefore probably mediates a majority of POMC-to-PVH<sup>MC4R</sup> cAMP signalling<sup>12,24,72,74</sup>. BIBP 3226<sup>67</sup> trifluoroacetate (NPY1R antagonist, Tocris, 2707, 4A/263489) was dissolved in ACSF with 10% DMSO at a concentration of 5 nmol  $\mu$ l<sup>-1</sup> and filtered (Millipore, Millex-GV, 0.22  $\mu$ m). BIBP 3226 was used in i.c.v. infusions (10 nmol per mouse). CGP 71683 hydrochloride (NPY5R antagonist, Tocris, 2199, 3B/275453) was dissolved in ACSF with 30% DMSO at a concentration of 5 nmol  $\mu$ l<sup>-1</sup> and filtered. CGP 71683<sup>68</sup> was used in i.c.v. infusions (10 nmol per mouse). SR 95531 hydrobromide (GABAzine, Tocris, 1262, 15A/280031) was dissolved in distilled H<sub>2</sub>O at 20 mM and used at a concentration of 20  $\mu$ M in whole-cell recordings. Kynurenic acid (Millipore-Sigma, K2272-5G, SLCN25759) was freshly dissolved in ACSF and used at a concentration of 1 mM.

### Chronic food restriction and switching between feeding states

Chronic food restriction was performed as previously described<sup>75,76</sup>. In the fasted state, mice were kept at 85% of ad libitum weight (weighed every morning before experiments) by restricting food access during and after experiments. Weight and food intake were logged per mouse per day. To reduce the discomfort of weight changes, most mice only went through one food-restriction/refeeding cycle to test fasted and ad libitum fed states. For mice that were used for multiple experiments (for example, testing different stimulation protocols, conducting both FLIM and non-FLIM imaging experiments), we also tried to minimize the confounding effects of time between fasted and fed states. To do so, we typically performed half of the ad libitum fed-state experiments first (for example, 2 out of 4 fed sessions), then all of the fasted-state experiments (for example, all four fasted sessions) and finally finished the ad lib fed-state experiments (for example, the remaining two fed sessions). We did not observe lasting effects of food restriction, with mice regaining full body weight within a day or two of ad libitum food access.

### Freely moving feeding assays

For food intake assays involving optogenetic and chemogenetic manipulations (Fig. 5e), the mice were singly housed immediately after the surgery and acclimatized to the handling and experimental setting for >1 hour per day for 5 consecutive days before the experiment. Food intake studies were performed at the onset of the dark cycle (zeitgeber time 12–15, when mice engage in normal dark-cycle feeding).

For chow-based feeding assays (Fig. 5e), food intake was measured at the 0, 1, 2 and 3 h timepoints. On the day of the experiment, the mice were attached to the patch cord (1 m length, NA 0.57, Doric Lenses) and injected with either saline or CNO (1 mg per kg) 30 min before the onset of the experiment. The light stimulation was delivered through light-emitting diodes (LEDs; Plexbright) at a peak power of 7–9 mW at the fibre tip. Optogenetic trains (20 Hz, 10 ms pulses, 1 s on, 3 s off) were generated using a custom-made TTL pulse generator. The light stimulation protocol began immediately before the onset of the first food measurement and continued for the 3 h duration of each food intake session.

For the liquid-diet (that is, Ensure) feeding assay (Fig. 5f), food intake was measured through a lick spout (details are provided below). Each lick triggers a pulse of Ensure, and we recorded the number of licks over an hour per mouse. The optogenetic stimulation protocol (20 Hz, 10 ms pulses, 1 s on, 3 s off) began immediately after the lick spout was inserted inside the cage (and therefore became accessible) and continued for the duration of each food intake session. We note that previous work<sup>11,47,62,77</sup> that used *Pomc-cre* mice mostly found no effects on feeding in the first many hours (but see ref. 78), while studies stimulating *Pomc-dre* neurons (ref. 46 and here) show a modest reduction in feeding in the first hour. We suspect that this discrepancy may be

# Article

explained by differences in the subsets of neurons labelled by each driver line and our choice to perform optogenetic stimulation of axons rather than somas.

## Freely moving 24 h feeding, body-length and body-weight measurements

For freely-moving 24 h feeding (Extended Data Fig. 1i), body-length (Extended Data Fig. 1e) and body-weight (Fig. 1c) measurements, animals were singly housed, and the body weight and 24 h food intake of individual animals were measured every week after AAV injection. Body weight was measured on day 1 of each week; 24 h food intake was measured for three consecutive days at the beginning of each week (days 1–3) and these values were averaged to account for daily variations in food intake.

For body-length measurements, animals were maintained in group housing with their original littermates throughout the duration of the experiment. Body length (nose-to-anus length) was measured every week after AAV injection during brief isoflurane anaesthesia.

## Indirect calorimetry and MRI

24 h food intake (LabDiet 5008, 3.56 kCal g<sup>-1</sup>), water intake, physical activity (beam breaks), oxygen consumption, carbon dioxide production and body mass of single-housed mice were measured every 2 min using the Sable Systems Promethion indirect calorimeter in the BIDMC Energy Balance Core. Mice were weighed and body compositions were scanned using an EchoMRI 3-in-1 body composition analyser (no anaesthesia) before they were placed in the Promethion system for recording. All of the mice were allowed 12 h of habituation in the system before the 72 h experiment. From the measurements, energy intake, energy expenditure, respiratory exchange ratio, physical activity and energy balance were calculated using CalR<sup>79</sup> (<https://calrapp.org/>).

## Head fixation with food delivery

Head fixation was used in photometry and two-photon microscopy experiments to record cAMP and calcium activity while reducing motion artifacts. The experiments were performed using head-fixed mice that could run freely on a circular treadmill equipped with IR beam breaks to record the speed<sup>76</sup>. For experiments involving food delivery, milkshake (Ensure Plus, 350 kCal per 236.59 ml (8 oz) bottle) was delivered through a lickspout<sup>76</sup>. The speed of food delivery was controlled by gravity and gated by solenoid pulses. Each pulse opened the solenoid for 150 ms, which resulted in 3 µl of milkshake delivery. For trial-based feeding experiments, we delivered 5 Ensure pulses (15 µl; Fig. 5a) or 10 Ensure pulses (30 µl; Extended Data Fig. 8d–o) per trial. For all head-fixed feeding experiments, there was a 4 min waiting period before the first trial to record baseline sensor activity and bleaching rate. All datasets were collected as triplicates per condition.

Food delivery during two-photon imaging was controlled using an Arduino ([https://github.com/xzhang03/Train\\_generator](https://github.com/xzhang03/Train_generator)). One session was performed per day. For two-photon imaging experiments in Fig. 5b, 10 trials were conducted per session at a rate of 1 trial per minute, and each trial used a 5-pulse train (300 ms between pulse onsets).

Food delivery during photometry or behavioural experiments was controlled using the Nanosec photometry-behavioural system (<https://github.com/xzhang03/NidaqGUI>). In the head-fixed refeeding assay, each lick triggers a pulse of Ensure, and we recorded the number of licks over an hour per mouse (Extended Data Fig. 8c). Low-level biPAC stimulation was performed by pulsing 465 light (50 µW) at a pulse-width of 6 ms and a frequency of 50 Hz, with a resulting power of 15 µW. Note that, during initial testing in brain slices, equal-light-intensity biPAC stimulation induced many-fold greater cAMP production than previously observed (for example, MPOA<sup>23</sup>), possibly due to a greater ATP concentration in PVH<sup>MC4R</sup> neurons. As such, we took care not to design biPAC experiments involving high light intensity to avoid over-stimulation and possible ATP depletion.

For photometry and head-fixed food intake experiments with trial structures (Fig. 6a and Extended Data Fig. 8d–o), 50 trials were conducted per session at a rate of 1 trial per minute and each trial used a 10-pulse train of Ensure deliveries (300 ms between Ensure pulse onsets, 3 µl per pulse, 30 µl total per trial). The increased number of trials and increased total Ensure delivery per trial during the photometry experiments was designed to partially satiate mice over the course of the experiment. For experiments using conditional food delivery (Extended Data Fig. 8f), a 2 kHz tone was played for 1 s, during which the mice must lick at least once to trigger the food delivery train. If triggered, the food delivery train started as soon as the tone was over. Otherwise, the mice must wait until the next trial (1 trial per min), and the current trial was omitted in the photometry analysis. At 10 pulses per train and 50 trains per session, the maximum amount of milkshake a mouse could consume there is 1.5 ml, which is approximately 50% of the absolute maximum volume that a mouse would consume in previous experiments<sup>75</sup>. For experiments involving biPAC stimulation, a 1 s light pulse (465 nm, 1 mW peak, 70% duty cycle) was delivered 5 s before the tone in 50% of the trials (randomly selected; Extended Data Fig. 8d). The 5 s delay was chosen to allow sufficient cAMP production before the tone (Extended Data Fig. 5c). To verify satiation, we also sometimes (at least once per mouse per condition) gave the mouse the choice to perform an additional 10 trials 10 min after the regular experiments (Extended Data Fig. 8f).

Mice were trained for around 2 weeks before each experiment, with the following sequence: (1) habituation to handling; (2) habituation to head-fixation; (3) habituation to food delivery via lick spout; and (4) operant conditioning assay (if applicable).

## Head-fixed photometry

Head-fixed photometry experiments were conducted as described previously<sup>23</sup> using mice running on a circular treadmill. For experiments using a green sensor (Axon-GCaMP6s), excitation light from a 465 nm LED (for fluorescent sensor excitation, ~100 µW peak) and a 630 nm LED (for optogenetic stimulation of Chrimson; 1 mW peak if used) were combined in a four-port fluorescence mini-cube (FMC4\_E(460-490)\_F(500-550)\_O(580-650)\_S, Doric) and transmitted to the implanted fibre via a patch cord (1 m length, NA 0.57, Doric). For biPAC stimulation during GCaMP6s recording (Extended Data Fig. 9e), biPAC stimulation was performed by transiently elevating the intensity of the 465 nm photometry LED light from ~100 µW to 1 mW. This light intensity should be sufficient to photoactivate biPAC, of which the half-saturation light intensity is about 30 µW mm<sup>-2</sup> (characterized previously<sup>23</sup>). For experiments using a red sensor (jRCaMP1a), excitation light from a 555 nm LED (for sensor excitation, ~100 µW peak) and a 465 nm LED (for optogenetic stimulation of biPAC; 1 mW peak if used) were combined in a five-port fluorescence mini-cube (FMC5\_E(450-490)\_F1(500-540)\_E2(550-580)\_F2(600-680), Doric) and transmitted to the implanted fibre through a patch cord (1 m length, NA 0.57, Doric). The emitted light was measured from the emission port of the mini-cube using a femtowatt photoreceiver (2151, Newport).

All photometry and optogenetic excitation lights were modulated as interleaved pulses controlled by the Nanosec photometry-behavioural system that was initially developed in a previous study<sup>23</sup> (<https://github.com/xzhang03/NidaqGUI>). Each cycle (20 ms per cycle, or 50 cycles per second) consists of (1) turning on the photometry (465 nm or 555 nm) LED for 6 ms (step 1) and then (2) turning off the photometry LED for 14 ms (step 2). If Chrimson stimulation was used, once every 5 cycles, the 630 nm LED was turned on immediately after step 2 and then turned off 10 ms later, which corresponds to 10 Hz, 10 ms pulses (duty cycle = 10%). If biPAC stimulation was used, once every cycle, the 465 nm LED was turned on immediately after step 2 and turned off 14 ms later, which corresponds to 50 Hz, 14 ms pulses (duty cycle = 70%). The recording was conducted in darkness. Black heat shrink was placed around the fibre to help prevent the LED light from being seen by

the mice. For 2 weeks before the photometry experiments, each mouse was habituated to handling and head fixation.

### Two-photon imaging

Two-photon imaging was performed using a two-photon resonant-galvo scanning microscope (NeuroLabWare) controlled by Scanbox (<https://scanbox.org/>) as described previously<sup>23,76</sup>. An InSight X3 laser (Spectra-Physics) was used to excite the fluorophores (910–1,050 nm), and the emission light was filtered (green: 510/84 nm; red: 607/70 nm; Semrock) before collection with photomultiplier tubes (H10770B-40; Hamamatsu). The *xy* scanning was performed using resonant/galvo mirrors and the *z* scanning was achieved using an electrically tuneable lens (Optotune).

2p-FLIM was enabled by modifying the existing two-photon microscope (NeuroLabWare). Both FLIM and the conventional two-photon imaging used the same excitation light path. In experiments involving FLIM, an extra beam-splitter (75 T/25R, Semrock) was added to the emission light path such that 75% of the emission light was directed to the standard intensity-based PMT (H10770B-40; Hamamatsu) and the rest (25%) was split to the FLIM light path. In the FLIM light path, the emission light was filtered (510/84 nm; Semrock) before entering the hybrid PMT (Becker and Hickl, HPM-100-40). PMT data were digitized using a time-correlated single-photon counting board (Becker and Hickl, SPC-150) to estimate photon counts and arrival times. Frames were constructed from the pixel and frame clocks in the NeuroLabWare microscope. Laser clocks were recorded with an independent photodiode (Becker and Hickl, PHD-400-N) in the excitation path. In the FLIM experiments, the laser intensity was controlled (<10 mW) so that the FLIM PMT received  $2.5\text{--}5 \times 10^5$  photons per second (to avoid cross-pulse photon contamination, see below). Each frame was collected from 2–5 s of continuous scanning so that it contained at least 1 million photons per  $\text{mm}^2$  to ensure accurate lifetime estimates while minimizing laser power.

### Two-photon imaging of fixed brain slices

To count the number of PDE4D3-Cat-expressing and mCherry-expressing cells in an automated manner<sup>80</sup>, we used the two-photon microscope to scan fixed brain slices that were stained with mCherry (594 nm excitation for secondary antibody). Brain slices (thickness, 60  $\mu\text{m}$ ) were prepared, and every other slice was mounted and then covered with a coverslip. The slices that contained the brain region of interest (that is, the PVH) were placed under a  $\times 16$  water-immersion objective (NA 0.8, CFI75LWD, Nikon), and were scanned at 15.5 fps and  $796 \times 512$  pixels per frame. We excited the fluorophores at 1,050 nm (5–15 mW). We collected 50 volumes (30 steps spanning 60  $\mu\text{m}$  per volume).

### Two-photon imaging of acute brain slices

Acute brain slices were prepared as described previously<sup>63</sup> and transferred to a recording chamber perfused with ACSF (oxygenated with 95%  $\text{O}_2$  and 5%  $\text{CO}_2$ ; flow rate: 2–5  $\text{ml min}^{-1}$ ) at room temperature. Two-photon imaging was performed using the same microscope and  $\times 16$  lens as described above. The excitation wavelength used was 910 nm.

In pharmacological experiments involving the NPY sensor npy-Light1.0, each slice was imaged for 15 min (15.5 fps) and 200 nM NPY (Tocris, 1153) was applied through perfusion starting at 4 min into the recording. In npyLight1.0 experiments that involve photostimulating AgRP axons in the PVH, each slice was imaged across four runs, with each run involving one optogenetic stimulation duration (2 s, 4 s, 8 s, 16 s). The order of the runs (that is, stimulation durations) was randomly selected between ascending order (2 s first and 16 s last) and descending order (16 s first and 2 s last) to average out potential history-dependent effects. In each run, at timepoints 2 min, 3 min, 4 min, 5 min and 6 min, a 655 nm LED (1  $\text{mW mm}^{-2}$ , Luxeon Star LEDs) driven by an Arduino-controlled driver (Luxeon Star LEDs) was used to deliver

photostimulation trains (<https://github.com/xzhang03/bPACstim>). The first 2 min of each run was used as the baseline. To protect the PMT during optogenetic stimulation, the photostimulation pulses were time-locked to the start of each frame (immediately after galvo flyback, resulting in 15.5 photostimulation pulses per second). During frames with optogenetic pulses, the PMT was blanked for 10 ms, and the LED was turned on for the first 8 ms (and leaving 2 ms for LED to turn off before unblanking the PMT). Using this method, the stimulation frequency is the same as the frame rate (15.5 Hz) and the duration is controlled by the frame number (for example, 2 s = 31 frames of stimulation). Note that npyLight1.0 will be published by the Tian group in a separate article.

In experiments involving biPAC stimulation, we used longer optogenetic pulses (that is, 100 ms) that cannot be synchronized to a single frame. Thus, to protect the PMT, we manually turned off PMT while biPAC stimulation was triggered.

### In vivo i.c.v. infusion

Owing to the close horizontal proximity of the cannula and the GRIN lens, we chose a minimal setup to perform i.c.v. infusions to not hinder the FOV or risk damaging the exposed lens. I.c.v. infusion was performed through a 22XX-gauge (two Xs in the manufacture specifications) cannula (MicroGroup, 0.6 mm ID, 0.72 mm OD, 6.99 mm length), a 1 ml syringe, an automated syringe pump (Harvard Apparatus, 70-4504), and the required tubing. When the cannulas were not used, they were plugged with a small piece of tubing that was secured with a silicone gel (Kwik-Cast). Before imaging, the plug was removed and the infusion tubing was inserted to a pre-calculated depth that did not protrude from the bottom of the cannula. The tubing was then sealed and secured with silicone gel. We regularly observed a small amount of back-flowing CSF when the plug was removed, indicating an unobstructed cannula. All parts were sterilized before being inserted into the cannula. The rest of the imaging setup was performed in the same manner as for the regular imaging experiments. During infusion, the rate was kept consistent at  $1 \mu\text{l min}^{-1}$  and the volume varied between 1 and 4  $\mu\text{l}$  as determined by the peptide dosage. We occasionally saw increased running when infusing 4  $\mu\text{l}$ , but no agitation or vocalization was noted. For peptides that are dissolved in ACSF/DMSO mixtures, same-ratio mixtures were used for the corresponding control experiments. We did not observe a noticeable impact of DMSO on cAMP.

### In vivo two-photon imaging experiments

In vivo two-photon imaging of the PVH via a GRIN lens in head-fixed mice was generally performed as described previously<sup>23,63</sup>. The excitation wavelength was 910 nm. The experiments were performed using head-fixed mice that could run freely on a circular treadmill<sup>76</sup>. Imaging was performed using a  $\times 4/0.2$  NA air objective (Nikon) in mice implanted with doublet GRIN lens (see above;  $\times 2.6$  magnification, NA 0.19 on the air side). Light-shield material was used to protect the lens and the objective from external light. Imaging FOVs were at a depth of 100–300  $\mu\text{m}$  below the face of the GRIN lens. The laser and frame parameters were described above. As cAMP changes relatively slowly<sup>23,35</sup>, we opted to simultaneously image 2–3 FOVs that were at least 60  $\mu\text{m}$  apart (using Optotune) to increase cell sampling and FOV counts at the expense of frame rate (effective frame rate = 10.3 Hz for a three-FOV session and 15.5 Hz for a two-FOV session). The FOVs were chosen to reduce repeated imaging of the same cells.

For the optogenetic experiments, we imaged for 15 min per session. Excitation light from a 617 nm LED (Thorlabs; M617L3) was focused into the GRIN lens using the same  $\times 4$  objective. The LED power was measured to be 2 mW below the  $\times 4$  objective and, based on previous experiments, around 50% of the power passes through the GRIN lens. Photostimulation trains were delivered at timepoints from 2 min to 11 min into the recording (10 trains, 1 min between train onsets). To protect the PMT during optogenetic stimulation, the photostimulation pulses were time-locked to the start of each frame (31 fps). During

frames with optogenetic pulses, the PMT was blanked for 10 ms, and the LED was turned on for the first 8 ms (leaving 2 ms for the LED to turn off before unblanking the PMT). Using this method, the stimulation frequency is the same as the frame rate (31 Hz) and the duration was controlled by the frame number (that is, 250 frames  $\approx$  8 s). This stimulation protocol is within the range of the stimulation parameters used in previous neuropeptide studies<sup>25,28,81</sup> and mimics the phasic firing patterns of the peptide-releasing neurons<sup>8</sup>. The effect of such stimulation protocols on the calcium activity of AgRP and POMC axons is shown in Extended Data Fig. 5a. In grouped stimulation experiments (Extended Data Fig. 6s–t), the time between train onsets was shortened from 1 min to 10 s while keeping all of the other stimulation parameters the same (including 8 s train lengths). This effectively resulted in a single prolonged train per session lasting 98 s in duration.

For optogenetic experiments that also used i.c.v. infusion of neuropeptide agonists or antagonists, the drugs were pre-infused through the cannula 10 min before imaging started. For optogenetic experiments that also used i.p. injections (such as MTII), the injection was performed 15 min before imaging.

For i.c.v. infusion experiments (Fig. 4b) or i.p. injection experiments (Extended Data Fig. 6a–e) without optogenetic stimulation, we imaged for 15 min per session, and the drugs were introduced at 3 min into the recording. In these experiments, because cAMP changes are slow, FLIM was also used, and the FLIM data were acquired at 1 frame (5 s acquisition) every 10 s throughout the session.

For feeding experiments, simultaneous FLIM and non-FLIM imaging datasets (20 min per session) were acquired as described above. FLIM data were used to determine the overall changes in absolute cAMP levels, while non-FLIM (that is, intensity-based imaging) data were used to visualize single-trial cAMP transients. FLIM data were acquired at 1 frame (5 s duration) every 10 s throughout the session. Non-FLIM imaging data were acquired at 15.5 fps and only one FOV was imaged per session. Uncued food deliveries started at 4 min, and 10 trials were presented (1 min between trial onsets) using the methods described above.

## Electrophysiology in acute slices

To prepare ex vivo brain slices, 6–10 week-old mice were deeply anaesthetized with isoflurane before decapitation and removal of the entire brain. The brains were immediately submerged in ice-cold, carbogen-saturated (95% O<sub>2</sub>, 5% CO<sub>2</sub>) choline-based cutting solution consisting of 92 mM choline chloride, 10 mM HEPES, 2.5 mM KCl, 1.25 mM NaH<sub>2</sub>PO<sub>4</sub>, 30 mM NaHCO<sub>3</sub>, 25 mM glucose, 10 mM MgSO<sub>4</sub>, 0.5 mM CaCl<sub>2</sub>, 2 mM thiourea, 5 mM sodium ascorbate, 3 mM sodium pyruvate, oxygenated with 95% O<sub>2</sub>/5% CO<sub>2</sub>, measured osmolality 310–320 mOsm l<sup>-1</sup>, pH 7.4. Then, 275–300- $\mu$ m-thick coronal sections were cut with a vibratome (Campden, 7000smz-2) and incubated in oxygenated cutting solution at 34 °C for 10 min. Next, slices were transferred to oxygenated ACSF (126 mM NaCl, 21.4 mM NaHCO<sub>3</sub>, 2.5 mM KCl, 1.2 mM NaH<sub>2</sub>PO<sub>4</sub>, 1.2 mM MgCl<sub>2</sub>, 2.4 mM CaCl<sub>2</sub>, 10 mM glucose) at 34 °C for an additional 15 min. The slices were then kept at room temperature (20–24 °C) for  $\geq$ 45 min until use. A single slice was placed in the recording chamber where it was continuously superfused at a rate of 3–4 ml per min with oxygenated ACSF. Neurons were visualized with an upright microscope (SliceScope Pro 1000, Scientifica) equipped with infrared-differential interference contrast and fluorescence optics.

Whole-cell patch-clamp recordings were performed with an intracellular solution containing 128 mM potassium gluconate, 10 mM KCl, 10 mM HEPES, 1 mM EGTA, 1 mM MgCl<sub>2</sub>, 0.3 mM CaCl<sub>2</sub>, 5 mM Na<sub>2</sub>-ATP, 0.3 mM Na-GTP (pH 7.3). A list of protocols is provided below:

(1) Action potential frequency, amplitude and membrane potential were assessed in current-clamp mode for a period of 2 min immediately after breakthrough.

- (2) The action potential threshold was assessed in current-clamp mode by first hyperpolarizing the membrane potential to a subthreshold level (–70 mV) and then injecting a current ramp (0–80 pA) for 2 s.
- (3) *I*–*V* relationships were assessed in current-clamp mode by first injecting sufficient current to reach a stable membrane potential of –70 mV and then stepping through additional current injection series ranging from –40 pA to +40 pA.
- (4) Assessment of sEPSCs was performed in voltage-clamp mode with recordings lasting at least 3 min after establishment of a stable baseline.
- (5) Input resistance and membrane capacitance were assessed in voltage-clamp mode by briefly hyperpolarizing the holding potential by –10 mV for 500 ms.

Cell-attached recordings (seal resistance 20–50 M $\Omega$ ) were made in voltage-clamp mode with the recording pipette filled with ACSF and holding current maintained at  $V_h$  = 0 mV. To photoactivate biPAC, an LED light source (470 nm) was used. The blue light was focused onto the back aperture of the microscope objective ( $\times$ 40), producing wide-field illumination around the recorded cell of 10–15 mW mm<sup>-2</sup> as measured using an optical power meter (PM100D, Thorlabs). A programmable pulse stimulator, Master-8 (A.M.P.I.), and pClamp 10.2 software (Molecular Devices, Axon Instruments) controlled the photostimulation output.

All recordings were made using a Multiclamp 700B amplifier, and data were filtered at 2 kHz and digitized at 20 kHz. Access resistance ( $<$ 30 M $\Omega$ ) was continuously monitored by a voltage step and recordings were accepted for analysis if changes were  $<$ 15%.

Pharmacological agents were freshly dissolved to working concentrations in ACSF and applied through the perfusion pump system (Multichannel dispenser pump, Ismatec).

## Histology

Perfusion and histology were performed as described previously<sup>82</sup>. Brain slices (thickness, 60  $\mu$ m) were collected and one of every three consecutive slices was scanned. The primary antibodies used in this paper are chicken anti-GFP (1:1,000, Invitrogen; used for GFP and GCaMP6s) and rat anti-mCherry (1:1000, Thermo Fisher Scientific; used for mCherry and tdTomato). The secondary antibodies are donkey anti-chicken 488 (1:1,000, Jackson) and donkey anti-rat 594 (1:1,000, Jackson).

**Analysis procedures.** All data analyses were performed using custom scripts in MATLAB (MathWorks), Python, ImageJ (NIH), SPC-Image (Becker and Hickl) and Prism (GraphPad).

## Analyses of head-fixed and freely moving feeding assays

For the head-fixed refeeding assay (Extended Data Fig. 8c), we plotted the mean cumulative lick number per mouse. The same was done for freely moving feeding assays with liquid diet. For the freely moving assays, we also quantified latency to the first lick, defined as the time between when the lickspout became accessible and when the animal licks for the first time in a session (Extended Data Fig. 8a). To quantify the bout structure of freely moving feeding behaviours, we operationally defined the end of a feeding bout as 5 s without licking. We use this definition to quantify interbout interval in Extended Data Fig. 8b.

Analysis of conditional head-fixed feeding assays was based on the lick rates of the mice during the tone window (1 s after tone onset) and reward window (10 s after reward delivery onset), regardless of trial success. A trial was marked as a success if a mouse licked at least once during the tone window. An ethogram of an example experiment is shown in Extended Data Fig. 8e. These parameters were averaged per mouse (that is, average of three sessions per condition) and per condition (Extended Data Fig. 8f). If biPAC stimulation was used, independent comparisons were made across the means of the (a) biPAC-stimulation



trials in experimental session, (b) no-stimulation trials in experimental session, and (c) control session (Extended Data Fig. 8i). For correlation analysis (Extended Data Fig. 8m), we analysed sequences of 10 consecutive trials (for example, trials 23–32), calculated the change in the feeding metric (for example, lick rate during cue) and correlated that value to the number of stimulation trials within that set of 10 trials.

### Analyses of head-fixed photometry experiments

Head-fixed photometry data were analysed as described previously<sup>23</sup> ([https://github.com/xzhang03/Photometry\\_analysis](https://github.com/xzhang03/Photometry_analysis)). Pulses that trigger the photometry LED (50 Hz, see above) were used to determine when the LED was on. For each pulse (6 ms), we took the median of the corresponding datapoints in the photodetector trace to quantify the photometry signal. This results in a 50 Hz trace, which we then filtered with a 10 Hz low-pass filter.

To estimate bleaching, we fitted the pre-stimulation data (first 4 min of each experiment) with a mono-exponential function and subtracted the estimated values from each timepoint in the photometry trace across the entire recording. As all photometry experiments have a trial structure, we used the baseline fluorescence (for example, the 10 s pre-stimulation window; Extended Data Fig. 5a) to estimate  $\Delta F/F_0$ . The  $\Delta F/F$  traces were then pooled across days and z-scored per mouse. To show single-trial photometry traces, we triggered photometry traces with cue onsets with a 10 s pre-cue baseline and a 50 s post-cue recording (an example experiment is shown in Extended Data Fig. 9a). For Fig. 6a, we grouped the calcium transients in bins of five trials to show the gradual progression of excitation.

### Pre-processing of two-photon imaging experiments

Image registration was performed in MATLAB using a two-step process: (1) a rigid xy-translation step that is repeated three times ([https://github.com/xzhang03/Tiff\\_preprocess\\_2023](https://github.com/xzhang03/Tiff_preprocess_2023)); and (2) a non-rigid registration step using the Demonsreg function (<https://github.com/xzhang03/Demonsreg-Oneshot>). For experiments that involve simultaneous imaging of multiple z-planes, each z-plane was registered independently. To extract cell bodies, we downsampled images spatially by a factor of two. Then, we used Cellpose (v.2.0)<sup>80</sup> to segment soma ROIs. Repeating somas from multiple FOVs were excluded during analysis. For fixed-slide imaging, the number of ROIs was reported as the number of somas expressing the markers. Note that this number probably reflects only 50% of the total cell counts, as we imaged every other slice.

To extract neurite ROIs, we retrained three built-in Cellpose models—cyto, nuclei and the base network—to manually labelled neurites in three steps on an NVIDIA RTX3080 GPU: (1) 100 iterations of a 31-image set; (2) 500 additional iterations of the same set; and (3) 2,000 iterations of a 119-image set. We eventually decided to use the nuclei-based neurite model for subsequent analyses. Training progress, segmentation results and the models are all deposited to a public repository ([https://github.com/xzhang03/cellpose\\_GRIN\\_dendrite\\_models](https://github.com/xzhang03/cellpose_GRIN_dendrite_models)). After segmenting neurites, neurite ROIs were then manually matched to somas of the same FOV for future analysis.

For cross-day experiments (Fig. 5b), soma-ROIs in the same FOV were also matched manually.

After segmentation, we calculated the fluorescence traces from soma and neurite ROIs, and subtracted from them the fluorescence traces of the surrounding neuropil rings. Neuropil rings were calculated by first dilating the ROI by 14 pixels and subtracting all ROIs from the dilated mask. If the resulting neuropil ring has fewer than 2,500 pixels, the process is repeated with incrementing dilating size. Mean neuropil traces were subtracted from the mean ROI trace at 1:1 scaling. The underlying assumption for the no-scaling subtraction is that if a given pixel contains photons from both the intended ROI (for example, the soma) and the neuropil, the neuropil photon contribution should be similar at the soma and the surrounding area. Thus, the subtraction was done to remove global influences from the estimation of neurons'

responses to stimulation. The traces were then triggered relative to the onset of optogenetic stimulation or food delivery, and the relative changes ( $\Delta F/F_0$ ) were calculated. We used a 20 s pre-stimulation and 110 s post-stimulation window to display most cAMP traces (Fig. 2f). The 110 s post-stimulation window was chosen to capture the entirety of non-persistent cAMP transients.

As cADDIS shows decreased fluorescence intensity when cAMP concentration increases, we plot cADDIS intensity changes on a flipped y axis ( $-\Delta F/F_0$ ) for presentation purposes. For estimates of persistence, trial-averaged traces with more than one hit event were excluded to avoid sustained cAMP signalling due to repeated hits (Extended Data Fig. 6q,r).

### Pre-processing two-photon FLIM data

Pre-processing of FLIM data was performed as described previously<sup>23</sup> and as briefly described below. Images were first preprocessed using SPCImage (Becker and Hickl). We used the first-moment method of estimating lifetimes<sup>23,83</sup>. The advantage of this method is its high signal-to-noise ratio (due to the lack of fit uncertainty) and robustness when the photon number is low. Moreover, to increase the accuracy of lifetime estimates, the first moment of each pixel was calculated after local, spatial binning (bin size:  $5 \times 5$  pixels,  $\sim 25 \mu\text{m}^2$ ; the size of the spatial binning was small compared to the typical size of a cell (1,500–2,000 pixels)). Furthermore, if the peak of the resulting decay histogram (256 bins in time, 48.86 fs per bin) had fewer than 5 photons, then that pixel was excluded from subsequent analyses. In this way, we obtained an image of photon counts and an image of estimated lifetimes at the resolution of the original frame ( $650 \times 550$  pixels for in vivo imaging through a GRIN lens and  $900 \times 550$  pixels for slice imaging).

The remainder of the data processing for FLIM experiments was performed in MATLAB ([https://github.com/xzhang03/SPC\\_analysis](https://github.com/xzhang03/SPC_analysis)). Both intensity and lifetime images were downsampled by a factor of two. Image registration was performed in the same manner as for the non-FLIM (intensity-based) datasets above, and the shifts were applied to lifetime images. Segmentation was performed using Cellpose (v.2.0)<sup>80</sup>. As a typical cell had a mean pixel intensity of 10–15 photons per pixel, its lifetime was estimated from  $\sim 20,000$ – $26,000$  photons. Neuropil-ring fluorescence intensity and lifetime traces were calculated as described previously<sup>23</sup> and subtracted from the soma data. Lifetimes are usually plotted as changes from the baseline, with the exception of Fig. 5b, in which changes are relative to the fasted baseline.

As cADDIS traces show decreased fluorescence lifetime when cAMP concentration increases, we plot their lifetime changes on a flipped y axis ( $-\Delta \text{lifetime}$ ) for presentation purposes.

### Classifier of cAMP increments and decrements

We found that, for any given cell, neuropeptide-mediated cAMP increments and decrements were unpredictable on a trial-by-trial basis, even when the same photostimulation protocol was used across trials. We therefore used a two-tailed classifier to determine hit trials (increments or decrements) or miss trials (no change in cAMP). Previous studies showed slow cAMP dynamics across many different brain areas<sup>23,35,50,84</sup>, so we assumed that cAMP also operates on a slow timescale in the PVH and pre-smoothed the single-trial cADDIS trials before classification. The classifier is based on the area under receiver operating characteristic curve (auROC) applied to  $\Delta F/F_0$  data from the pre-stimulation baseline and the post-stimulation period. The unit of classification is a single trial of a single ROI. The pre-stimulation window is defined as the last 20 s before stimulation or food delivery. The post-stimulation window is defined as a 30 s window after stimulation or food delivery, and the window onset is different for cADDIS and npyLight1.0 experiments. Longer windows were used for the grouped stimulation experiment (Extended Data Fig. 6s,t). An auROC value greater than 0.995 or less than 0.005 indicates that there is at most a 1% chance that the pre-stimulation and the post-stimulation datapoints are drawn from the same

distribution (that is, the null hypothesis). Trials with  $\text{auROC} > 0.995$  or  $\text{auROC} < 0.005$  were treated as hits, and then further differentiated into increments (post-stimulation cAMP > pre-stimulation cAMP) or decrements (post-stimulation cAMP < pre-stimulation cAMP). Within each group, the trials were sorted by their agonist response. Note that, even though the classifier is two-tailed, POMC neuron stimulation drove mostly cAMP increments (>12% of the trials, versus <1% for decrements) while AgRP neuron stimulation drove mostly cAMP decrements (>20%, versus <1% for increments), consistent with previous biochemical characterizations<sup>5,18,19,85</sup>. Following the classification, we show means of hits and misses. Whenever appropriate, we also show means across all trials as well (Extended Data Fig. 2d). Note that, because the classifier uses fixed windows to reduce false-positive hits, we did not assess spontaneous changes in cAMP.

Owing to the serendipitously large estimated cAMP changes in PVH<sup>MC4R</sup> neurons compared with previous experiments<sup>23,35</sup> as well as the bimodal nature of the amplitude of these changes (Fig. 2c), classifier outcomes were not sensitive to classifier thresholds in non-pharmacological experiments. However, for experiments involving the application of neuropeptide agonists and antagonists, the amplitudes of cAMP increments and decrements did shrink closer to 0, and the hit–amplitude distribution (usually Gaussian) could at times become truncated (Extended Data Fig. 2m). We suspect that, in these experiments, cAMP changes were closer to the detection threshold of cADDis ( $K_d$  of around 20  $\mu\text{M}$ )<sup>86</sup>. We nevertheless kept the classification parameters the same for consistency. In these experiments, adjusting the classification thresholds did not qualitatively affect the results.

To calculate the log distribution of peak/trough  $\Delta F/F_0$  values (Fig. 2c (inset)),  $\Delta F/F_0$  values were first offset by the baseline values. An additional small offset (0.001 or –0.001) was then added to remove zeros, which would otherwise give infinity in a log function. The natural log function was then applied to the resulting values, from which the distribution was generated. For hits-only distribution of  $\Delta F/F_0$  and area-under-curve values in Extended Data Fig. 4h, no offsets or log functions were used to enable more accurate cross-condition comparisons.

To calculate the fraction of peptide transmission that is blocked by an antagonist, we considered potential impacts on both the occurrence and amplitude of cAMP transients. For example, in Fig. 2r,s, co-blocking NPY1R and NPY5R reduced cAMP decrement frequency by 71% and reduced decrement amplitude by 66%, reflecting a 90% reduction in overall peptide transmission. The logic is described below:

$$\begin{aligned} &[\text{Percentage drop in cAMP signalling}] \\ &= 100\% - [\text{remaining cAMP signal after antagonist}] \\ &= 100\% - [\text{percentage of hits remaining}] \\ &\quad \times [\text{hit amplitude normalized to before antagon.}] \\ &= 100\% - (100\% - [\text{percentage drop in hit rate}]) \\ &\quad \times (100\% - [\text{percentage drop in hit amplitude}]) \\ &= 100\% - (100\% - 71\%) \times (100\% - 66\%) = 90.1\% \end{aligned}$$

## The dice model of hits and misses

Stochasticity analysis was inspired by a previous study of coin-toss-like behavioural choices in *Drosophila*<sup>87</sup> and studies of quantal release<sup>88</sup>. The key property of the dice-roll or coin-toss model is that the probability of obtaining an outcome (for example, cAMP increment) is the same from trial to trial. One ramification of this assumption is that, given the unitary event probability ( $P_1$ ), the chance of seeing 2, 3, ...,  $n$  outcomes in a row must follow the power function  $P_n = P_1^n$ . We used this mathematical function to construct dice plots such as in Fig. 2d. One disadvantage of this plot is that the chance of seeing 3 or more events in a row is close to zero (while still following the power function), so we also constructed linearized dice plots using the function  $\text{Ln}(P_n) = n \times \text{Ln}(P_1)$ , where Ln is the natural logarithm function (and could be a log function

of any base). The downside of this linearized model is that it amplifies noise in small probabilities.

In our experiments, stimulating AgRP axons evoked cAMP transients more frequently than stimulating POMC axons. This difference in the apparent transmission probability probably depends on factors such as axon excitability, bouton density, dense-core vesicle availability within each bouton and release probability. Moreover, the simultaneous inhibition of AgRP neurons and excitation of POMC neurons during feeding probably function as two independent sources of cAMP increments, resulting in a compounded transient rate (Extended Data Fig. 7d,e) that is higher than that induced by either alone (Fig. 2d,n).

## Correlation of cAMP and NPY changes between ROIs

Correlation of binary events (hits or misses) between different ROIs was generally calculated using the XNOR (exclusive not-or) function (the truth table is shown in Extended Data Fig. 4t), because this function does not give invalid values to sequences that lack a single hit. The disadvantage is that the estimation of the chance level of correlation needs to be calculated on a case-by-case basis, which we did through bootstrapping. We also verified the main conclusions with an independent method, F1 score<sup>89</sup> (also referred to as Dice correlation), as well as Pearson correlation of  $\Delta F/F_0$  values.

For analyses that also involve distance between ROIs, we used intercentroid distances and adjusted for GRIN lens magnification ( $\times 2.6$  magnification for doublets) as needed for in vivo experiments. For slice experiments (npvLight1.0), no GRIN lens was used so we did not apply the same magnification factor.

## Kymograph of soma and neurite hits

In Extended Data Fig. 4i, the presence of bipolar cell morphology with two clear, continuous neurites affords us a rare chance to use a kymograph to show the decorrelation between soma and neurite hits. Owing to the low signal-to-noise ratio of this method, we used additional low-pass filtering on the traces (0.2 Hz filter).

## Electrophysiological analysis

Cell-attached spike recordings and whole-cell sEPSC recordings were analysed using MATLAB by finding local peaks with predetermined thresholds on current, charge (time-domain integral of current) and widths ([https://github.com/xzhang03/ephys\\_analysis\\_2023](https://github.com/xzhang03/ephys_analysis_2023)). The results were spot-checked manually to ensure fidelity.

In current-clamp mode, the membrane potential was estimated using a moving-median filter that removes spikes and after-potentials. The threshold was estimated by finding the inflection point during the current injection ramp at which voltage-gated sodium channels are activated. As these two parameters were frequently recorded from the same cells, we also reported the difference between the two to calculate the fraction of cells with suprathreshold membrane potentials. We note that, because we did not always record spontaneous firing and threshold from the same cells, the exact percentages of suprathreshold cells and spontaneously firing cells differ.

Input resistance was estimated using Ohm's law ( $R_{\text{input}} = \Delta V/\Delta I$ ) on the voltage-clamp data when a –10 mV hyperpolarizing step was applied. Membrane capacitance was calculated from the charge transfer following the downward edge of the hyperpolarizing step using the equation  $C_m = \Delta Q/\Delta V$ .

## Statistics and reproducibility

Two-tailed  $t$ -tests and ANOVA were performed using Prism. For ANOVA, multiple-comparison correction was performed using the Šidák post hoc correction. For behavioural, metabolic and photometry results, each mouse (typically averaged across three tests) was treated as an independent sample. For two-photon experiments, each FOV was treated as an independent sample (2–5 FOVs per mouse), as done previously<sup>23</sup>. For non-fractional data, error bars show the s.e.m., using the

units reported in figure legends. Note that, for the purpose of illustration, the hits-only traces (Fig. 2f) use the per-hit s.e.m. error bars in plots, but hypothesis testing was performed using each FOV as an independent sample (Fig. 2g). Fractional analysis of hits and misses was done in MATLAB and used the total number of trials multiplied by the number of ROIs as the denominators. Hit rates were estimated through fitting using the linearized dice model (Extended Data Fig. 2b). For bar plots of hit rates, error bars show the 95% confidence interval of 100,000 iterations of bootstrapping the data (with replacement) and fitting the dice model per iteration (Extended Data Fig. 2c). As these bar graphs report fractions, no individual datapoints are plotted. Hypothesis testing between fractional data (for example, between hit rates) was performed using bootstrapping with the null-hypothesis being data from different conditions that were drawn from the same pool. For histology, representative images were shown in Extended Data Figs. 2f and 3d (each repeated three times for three mice). For all tests, not significant means that the null hypothesis cannot be rejected (that is,  $P \geq 0.05$ ), and significance in each figure is indicated by asterisks; \* $P < 0.05$ , \*\* $P < 0.01$ , \*\*\* $P < 0.001$ . The exact  $P$  values are reported in Supplementary Table 1.

## Reporting summary

Further information on research design is available in the Nature Portfolio Reporting Summary linked to this article.

## Data availability

Raw two-photon imaging and two-photon fluorescence imaging datasets are available from the corresponding authors on request. Source data are provided with this paper.

## Code availability

The custom analysis codes and designs in this paper are publicly available at GitHub (<https://github.com/xzhang03/Code-for-Zhang-and-Kim-et-al/>).

61. Chen, Y., Lin, Y.-C., Zimmerman, C. A., Essner, R. A. & Knight, Z. A. Hunger neurons drive feeding through a sustained, positive reinforcement signal. *eLife* **5**, e18640 (2016).
62. Atasoy, D., Betley, J. N., Su, H. H. & Sternson, S. M. Deconstruction of a neural circuit for hunger. *Nature* **488**, 172–177 (2012).
63. Lutas, A. et al. State-specific gating of salient cues by midbrain dopaminergic input to basal amygdala. *Nat. Neurosci.* **22**, 1820–1833 (2019).
64. Singh, U. et al. Neuroanatomical organization and functional roles of PVN MC4R pathways in physiological and behavioral regulations. *Mol. Metab.* **55**, 101401 (2022).
65. McHugh, T. J. et al. Dentate gyrus NMDA receptors mediate rapid pattern separation in the hippocampal network. *Science* **317**, 94–99 (2007).
66. Tong, Q., Ye, C. P., Jones, J. E., Elmquist, J. K. & Lowell, B. B. Synaptic release of GABA by AgRP neurons is required for normal regulation of energy balance. *Nat. Neurosci.* **11**, 998–1000 (2008).
67. Iyengar, S., Li, D. L. & Simmons, R. M. A. Characterization of neuropeptide Y-induced feeding in mice: do Y1–Y6 receptor subtypes mediate feeding? *J. Pharmacol. Exp. Ther.* **289**, 1031–1040 (1999).
68. Lecklin, A. et al. Receptor subtypes Y1 and Y5 mediate neuropeptide Y induced feeding in the guinea-pig. *Br. J. Pharmacol.* **135**, 2029–2037 (2002).
69. Criscione, L. et al. Food intake in free-feeding and energy-deprived lean rats is mediated by the neuropeptide Y5 receptor. *J. Clin. Invest.* **102**, 2136–2145 (1998).
70. Rossi, M. et al. A C-terminal fragment of agouti-related protein increases feeding and antagonizes the effect of alpha-melanocyte stimulating hormone in vivo. *Endocrinology* **139**, 4428–4431 (1998).
71. Fan, W., Boston, B. A., Kesterson, R. A., Hruby, V. J. & Cone, R. D. Role of melanocortinergic neurons in feeding and the agouti obesity syndrome. *Nature* **385**, 165–168 (1997).
72. Millington, G. W. M. The role of proopiomelanocortin (POMC) neurons in feeding behaviour. *Nutr. Metab.* **4**, 18 (2007).
73. Tung, Y. L., Piper, S. J., Yeung, D., O’Rahilly, S. & Coll, A. P. A comparative study of the central effects of specific POMC-derived melanocortin peptides on food intake and body weight in Pomc null mice. *Endocrinology* **147**, 5940–5947 (2006).
74. Hentges, S. T., Otero-Corchon, V., Pennock, R. L., King, C. M. & Low, M. J. Proopiomelanocortin expression in both GABA and glutamate neurons. *J. Neurosci.* **29**, 13684–13690 (2009).
75. Livneh, Y. et al. Homeostatic circuits selectively gate food cue responses in insular cortex. *Nature* **546**, 611–616 (2017).
76. Burgess, C. R. et al. Hunger-dependent enhancement of food cue responses in mouse postnatal cortex and lateral amygdala. *Neuron* **91**, 1154–1169 (2016).

77. Zhan, C. et al. Acute and long-term suppression of feeding behavior by POMC neurons in the brainstem and hypothalamus, respectively. *J. Neurosci.* **33**, 3624–3632 (2013).
78. Wei, Q. et al. Uneven balance of power between hypothalamic peptidergic neurons in the control of feeding. *Proc. Natl. Acad. Sci.* **115**, E9489–E9498 (2018).
79. Mina, A. I. et al. CalR: a web-based analysis tool for indirect calorimetry experiments. *Cell Metab.* **28**, 656–666 (2018).
80. Pachitariu, M. & Stringer, C. Cellpose 2.0: how to train your own model. *Nat. Methods* **19**, 1634–1641 (2022).
81. Wang, H. et al. A tool kit of highly selective and sensitive genetically encoded neuropeptide sensors. *Science* **382**, eabq8173 (2023).
82. Garfield, A. S. et al. Dynamic GABAergic afferent modulation of AgRP neurons. *Nat. Neurosci.* **19**, 1628–1635 (2016).
83. Yasuda, R. Imaging spatiotemporal dynamics of neuronal signaling using fluorescence resonance energy transfer and fluorescence lifetime imaging microscopy. *Curr. Opin. Neurobiol.* **16**, 551–561 (2006).
84. Massengill, C. I. et al. Sensitive genetically encoded sensors for population and subcellular imaging of cAMP in vivo. *Nat. Methods* **19**, 1461–1471 (2022).
85. Bernard, A. et al. MRAP2 regulates energy homeostasis by promoting primary cilia localization of MC4R. *JCI Insight* **8**, e155900 (2023).
86. Tewson, P. H., Martinka, S., Shaner, N. C., Hughes, T. E. & Quinn, A. M. New DAG and cAMP sensors optimized for live-cell assays in automated laboratories. *J. Biomol. Screen.* **21**, 298–305 (2016).
87. Zhang, S. X., Miner, L. E., Boutros, C. L., Rogulja, D. & Crickmore, M. A. Motivation, perception, and chance converge to make a binary decision. *Neuron* **99**, 376–388 (2018).
88. Korn, H. & Faber, D. S. Quantal analysis and synaptic efficacy in the CNS. *Trends Neurosci.* **14**, 439–445 (1991).
89. Goutte, C. & Gaussier, E. in *Advances in Information Retrieval* (eds Losada, D. E. & Fernández-Luna, J. M.) 345–359 (Springer, 2005); [https://doi.org/10.1007/978-3-540-31865-1\\_25](https://doi.org/10.1007/978-3-540-31865-1_25).
90. Bock, A. et al. Optical mapping of cAMP signaling at the nanometer scale. *Cell* **182**, 1519–1530 (2020).
91. Anton, S. E. et al. Receptor-associated independent cAMP nanodomains mediate spatiotemporal specificity of GPCR signaling. *Cell* <https://doi.org/10.1016/j.cell.2022.02.011> (2022).
92. Zaccolo, M., Zerio, A. & Lobo, M. J. Subcellular organization of the camp signaling pathway. *Pharmacol. Rev.* **73**, 278–309 (2021).
93. Bacskaï, B. J. et al. Spatially resolved dynamics of cAMP and protein kinase A subunits in aplysia sensory neurons. *Science* **260**, 222–226 (1993).
94. Fuxe, K. et al. On the role of volume transmission and receptor–receptor interactions in social behaviour: focus on central catecholamine and oxytocin neurons. *Brain Res.* **1476**, 119–131 (2012).
95. Klapoetke, N. C. et al. Independent optical excitation of distinct neural populations. *Nat. Methods* **11**, 338–346 (2014).

**Acknowledgements** We thank J. Resch, D. Atasoy, Y. Livneh, H. Fenselau, J. Brünig, O. Yizhar, M. Frank, V. Jayaraman, M. Crickmore, D. Rogulja, B. Sabatini, A. Banks, L. Tsai, J. S. Alvarado, H. Kucukdereli, M. Porneice, R. Essner, C. Massengill and the members of the Andermann and Lowell laboratories for feedback; M. Hammell, J. Baker, S. Sankar, J. Chen, P. Prasad, D. Guarino, H. Choh and A. Sambangi for helping with animal care, behavioural experiments and histology; O. Amsalem for technical support with refining Cellpose2.0 models; and C. Massengill for help with the jRCaMP1a test. N. Biglari and J. Brünig generated POMC-Dre mice. H. Fenselau provided the unpublished Dre-dependent ChR2 AAV. Boston Children’s Hospital Viral Core (NIH P30 EY012196) and HMS Research Instrumentation Core provided viral and laser printing services, respectively. M. Cortopassi and A. Banks at the BIDMC Energy Balance Core performed the energy-balance and body-composition experiments and helped with analyses. The authors were supported by a Lefler Fellowship, a Charles A. King Trust Fellowship and NIH K99 DK134853 (S.X.Z.); NIH T32 DK007529 (A.K.); NIH F32 DK112589 and T32N SO07484 (A.L.); NIH T32 GM007753, T32 GM144273, T32 HL007901 and F30 DK131642 (P.N.K.); NIH U01 NS115579 and U19 NS123719 (L.T.); NIH R01 DK096010, R01 DK075632, R01 DK089044, R01 DK122976, P30 DK046200 and P30 DK057521 (B.B.L.); NIH DP2 DK105570, R01 DK109930, DP1 AT010971, R01 MH12343, a McKnight Scholar Award, and grants from the Boston Nutrition and Obesity Research Center (P30 DK046200), the Klarman Family Foundation, the Pew Innovation Fund and a Charles Robert Broderick III Phytocannabinoid Research Grant (M.L.A.).

**Author contributions** S.X.Z. and M.L.A. conceived the project and wrote the manuscript with methodological and editing inputs from all of the authors. S.X.Z., A.K. and A.L. conducted all surgeries. A.K. generated and maintained multi-transgene mice. A.K. and P.S.S. performed the free-moving feeding experiments and related measurements. S.X.Z., L.F.C. and P.K.Z. performed photometry experiments. S.X.Z., A.K., P.S.S. and P.K.Z. performed in vivo two-photon imaging experiments, with technical help with i.c.v. infusion from P.N.K.; S.X.Z. and A.L. performed slice imaging experiments. J.C.M. performed electrophysiology experiments. A.K., L.F.C. and P.K.Z. performed all histology. Y.J., A.P. and L.T. developed nptLight1.0. S.X.Z., A.K., J.C.M., A.L., B.B.L. and M.L.A. analysed all data.

**Competing interests** The authors declare no competing interests.

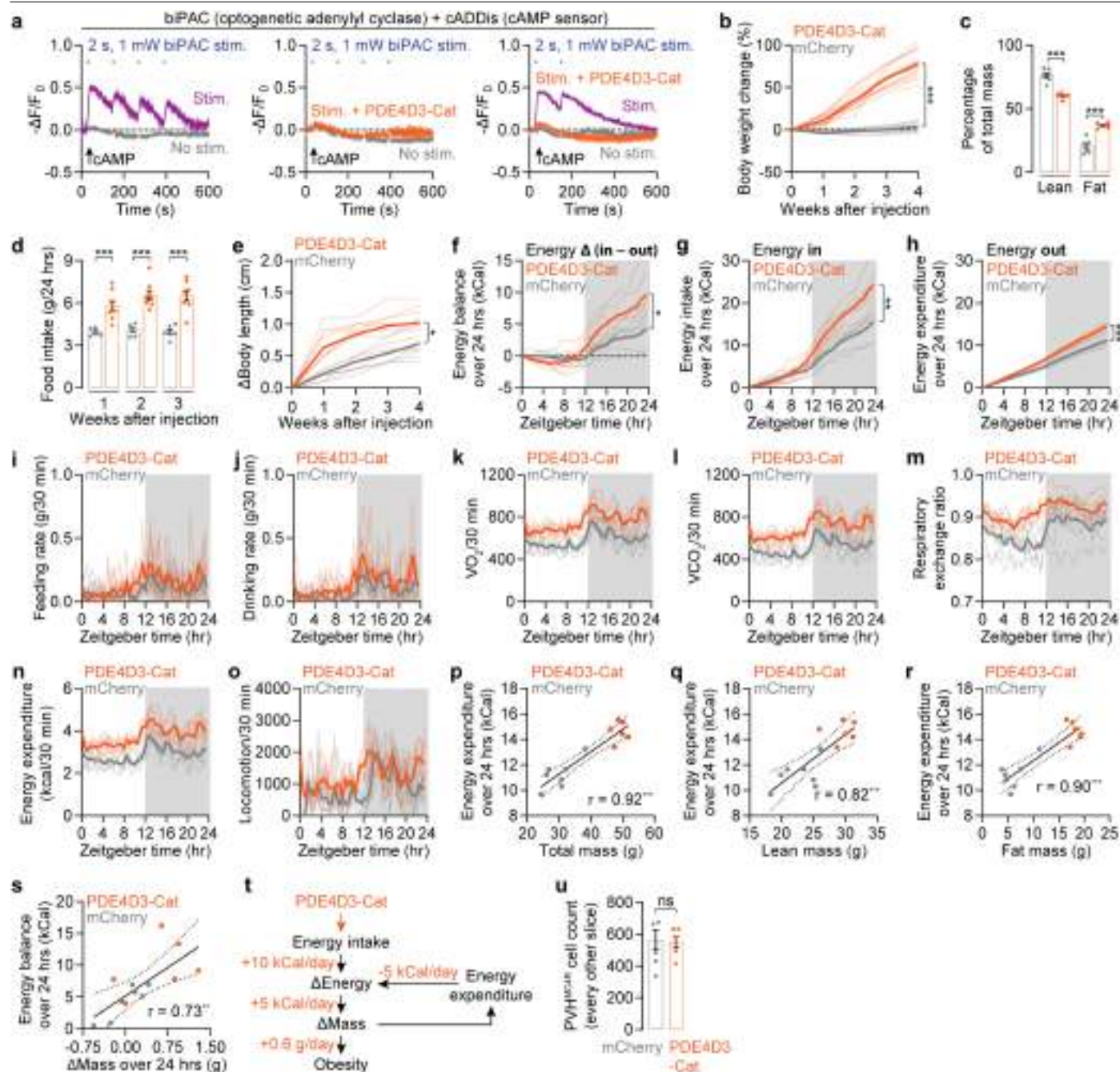
## Additional information

**Supplementary information** The online version contains supplementary material available at <https://doi.org/10.1038/s41586-024-08164-8>.

**Correspondence and requests for materials** should be addressed to Stephen X. Zhang or Mark L. Andermann.

**Peer review information** Nature thanks Richard Palmer and the other, anonymous, reviewer(s) for their contribution to the peer review of this work. Peer reviewer reports are available.

**Reprints and permissions information** is available at <http://www.nature.com/reprints>.

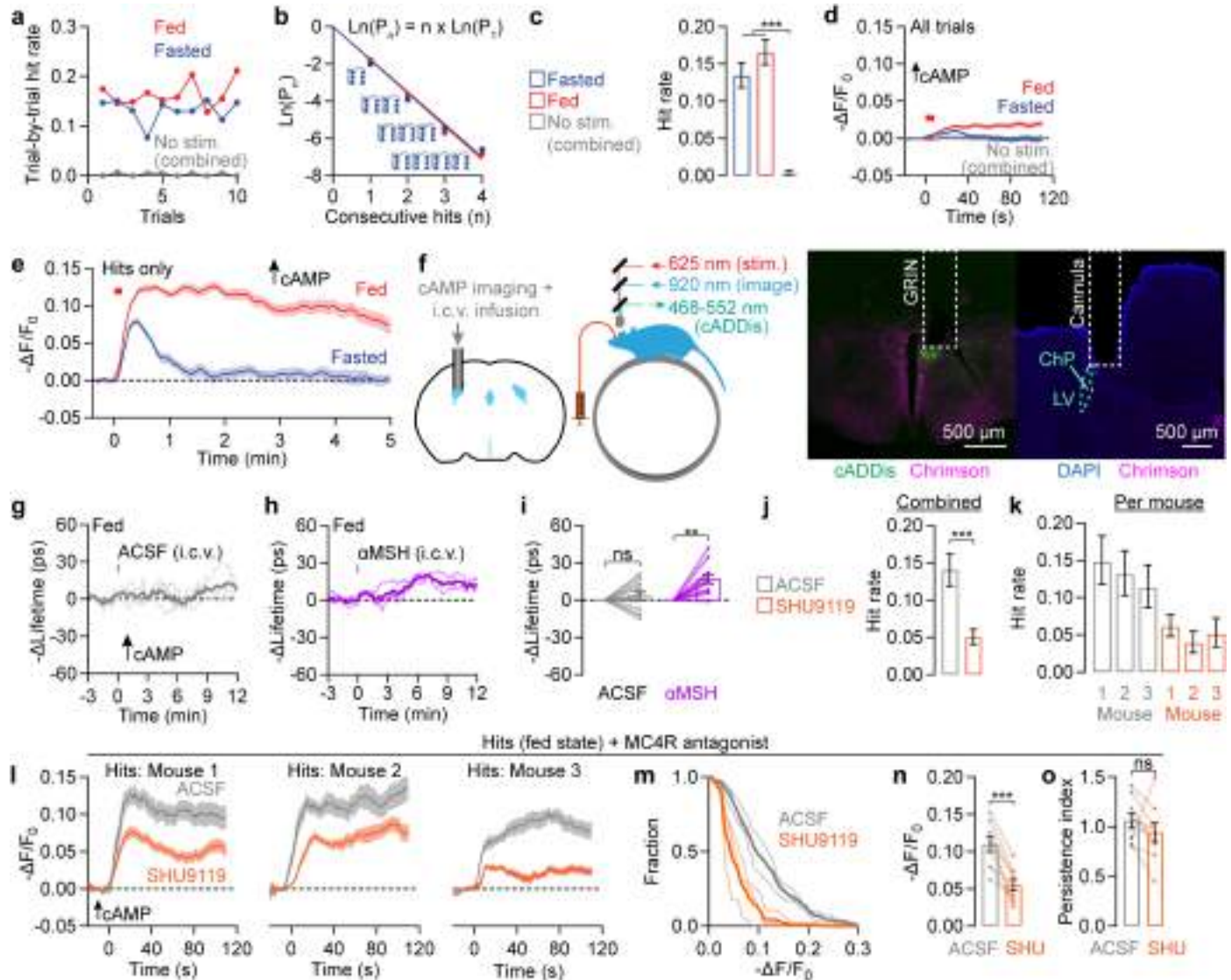


Extended Data Fig. 1 | See next page for caption.



**Extended Data Fig. 1 | Metabolic changes in mice expressing PDE4D3-Cat in PVH<sup>MC4R</sup> neurons.** (a) In acute brain slices, brief activation of a light-activated adenylyl cyclase with minimal dark activity, biPAC<sup>23</sup> (2 s, 1 mW), induced cAMP increments in PVH<sup>MC4R</sup> neurons that gradually decay back to baseline. Co-expressing PDE4D3-Cat, a constitutively active PDE selective for cAMP, completely blocked biPAC-induced cAMP transients and therefore should also reduce feeding-related cAMP increments. cADDis is a cAMP sensor<sup>86</sup>. n = 3-6 slices from 3 mice. (b) AAV expression of PDE4D3-Cat in PVH<sup>MC4R</sup> neurons in adult mice resulted in ~80% weight gain in the 4 weeks following surgery (n = 9-15 mice). For this and subsequent panels, the injection was performed when mice were eight weeks of age. (c) Mice that express PDE4D3-Cat had an elevated contribution of fat mass to their body composition (n = 6-7 mice). (d) PDE4D3-Cat expression in PVH<sup>MC4R</sup> neurons in adult mice resulted in hyperphagia in the 3 weeks following surgery (n = 6-8 mice). (e) PDE4D3-Cat expression in PVH<sup>MC4R</sup> neurons in adult mice resulted in ~0.5 cm increase in axial length in the 4 weeks following surgery (n = 7-8 mice). (f-o) To investigate the relative contributions of increased energy intake and decreased energy expenditure as causes of obesity, we used an indirect calorimetry system to measure these two factors independently (CalR<sup>79</sup>). Four weeks after surgery, PDE4D3-Cat-expressing mice accumulated a ~5 kCal energy surplus per day

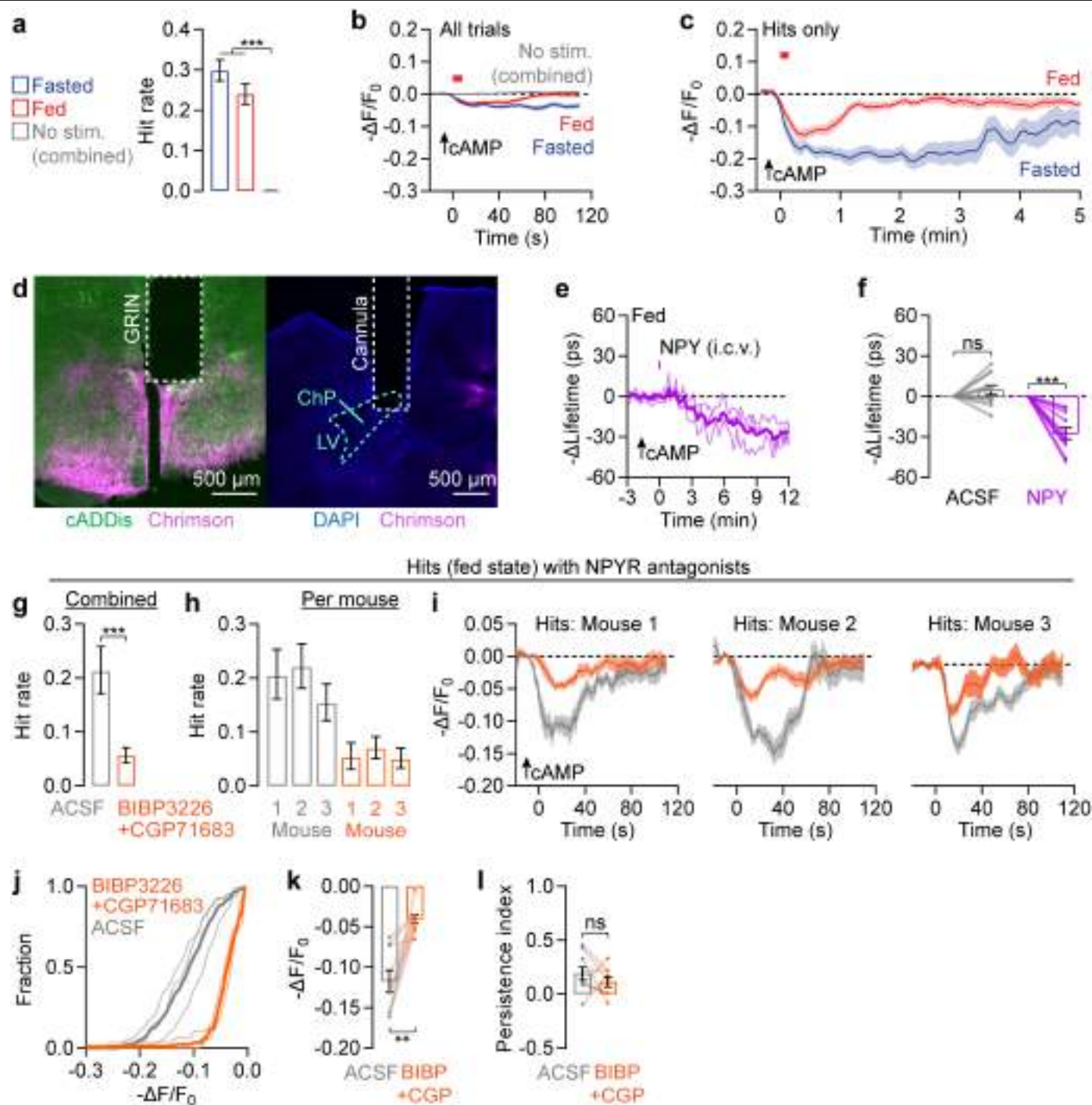
compared to littermates (f), resulting in the observed weight gain. However, rather than this net energy gain deriving from both increased energy intake and decreased expenditure, it was a result of elevated food intake (~10 kCal/day) that was insufficiently offset by elevated energy expenditure (~5 kCal/day) (g-h). The excess energy intake was primarily driven by elevated dark-phase feeding (i-j). The elevated energy expenditure, which is calculated from O<sub>2</sub> and CO<sub>2</sub> measurements (k-m), was evident throughout the day (n-o). All data are plotted in 30-min bins. Grey shading: dark phase of light-dark cycle. n = 6-7 mice. (p-s) Across individual mice, energy expenditure is well correlated with total mass (p), lean mass (q), and fat mass (r). Energy balance is correlated with change in mass (s), in the presence (orange) as well as in the absence (grey) of PDE4D3-Cat expression. n = 6-7 mice. (t) Diagram of energy gain: PDE4D3-Cat expression results in increased energy intake (10 kCal/day) that is only partially offset by elevated energy expenditure (5 kCal/day), resulting in a net 5 kCal/day surplus which translates to 0.6 g/day of weight gain. Hence, mice become obese over time. (u) PDE4D3-Cat expression did not affect PVH<sup>MC4R</sup> cell counts (n = 6-7 mice). a, c, d, u: mean ± s.e.m. across slices (a) and mice (c, d, u). c: one-way ANOVA; d: one-way ANOVA with data in Fig. 1e; e, f, g, h, u: unpaired t-test. ns, not significant, \*p < 0.05, \*\*p < 0.01, \*\*\*p < 0.001 for all figures. See Supplementary Table 1 for statistical details and sex-specific characterizations.



### Extended Data Fig. 2 | Characterizing $\alpha$ MSH signalling to PVH<sup>MC4R</sup> neurons.

(a-b) Hit rates showed no clear trends of increase or decrease across the session (a), indicating a fixed hit rate per trial. In such a model, if the probability of rolling a hit ( $P_1$ ) is known, the chance of observing two, three, or  $n$  consecutive hits is simply the product of the probabilities ( $P_1^2$ ,  $P_1^3$ , and  $P_1^n$ , respectively). In our data, the probability of observing several consecutive cAMP increments fits such a power function ( $P_n = [P_1]^n$ ). In b, y-axis is on a log scale to demonstrate the linearized version of the power function ( $\ln(P_n) = n \times \ln[P_1]$ , where  $\ln$  is the natural logarithm function). No-stimulation control trials show almost no hits.  $n = 1571$  fasted, 1836 fed, and 3176 no-stimulation trials from 4 mice. (c) Mean hit rates of POMC axon stimulation-induced cAMP increments in PVH<sup>MC4R</sup> neurons were not different between fasted and fed states. No-stimulation conditions in both fasted and fed states showed a low hit rate.  $n = 1571$  fasted, 1836 fed, and 3176 no-stimulation trials from 4 mice. (d) Across all trials, cAMP increments were greater in amplitude and more persistent in the fed state than the fasted state ( $n = 1571$  fasted and 1836 fed trials from 4 mice). (e) cAMP increments lasted more than 5 min in fed mice and 1-2 min in fasted mice.  $n = 211$ -304 hits from 4 mice. (f) Histology of cADDIs expression (green) in PVH<sup>MC4R</sup> neurons and Chrimson-tdTomato expression (red) in POMC axons. In the left panel, dotted lines delineate GRIN lens track. In the right panel, white dotted line delineates the anterior side of the infusion cannula inserted in the lateral ventricle (LV; cyan dotted line) which contains choroid plexus (ChP). We chose i.c.v. infusion of peptide antagonist/agonists here and below because many of these drugs do

not cross the blood-brain barrier. Similar histology results are obtained from all 3 mice. (g-h) We used two-photon fluorescence lifetime imaging microscopy (2p-FLIM), a photobleaching-insensitive imaging technique that is well-suited for tracking sensor fluorescence across slow timescales<sup>83</sup>, to track cAMP changes following i.c.v. infusion of  $\alpha$ MSH. We verified that i.c.v. infusion of  $\alpha$ MSH (1 nmol in 2  $\mu$ l, see Methods) induced a robust increase in cAMP in PVH<sup>MC4R</sup> neurons over ~8 min (h). No changes were seen after ACSF infusion (g).  $n = 3$  mice. (i) Summary of cAMP increases in PVH<sup>MC4R</sup> neurons across fields of view (FOV) in response to  $\alpha$ MSH infusion ( $n = 11$  FOVs from 3 mice). Lifetime changes are averaged from the 6-9 min window. (j) Pre-infusing MC4R antagonist SHU9119 (1 nmol) reduced the hit rate of POMC axon stimulation-induced cAMP increments in PVH<sup>MC4R</sup> neurons ( $n = 1401$ -2249 trials from 3 mice). (k) Same as j but showing per-mouse data ( $n = 421$ -921 trials per mouse per condition). (l) Per-mouse analyses of mean cAMP transients during hit trials after ACSF or SHU9119 (SHU) injections ( $n = 25$ -72 hits per mouse per condition). (m) Cumulative distribution of the magnitude of single-trial cAMP increments (measured with cADDIs) indicates a reduction in magnitude when SHU9119 was pre-infused before optogenetic stimulation of POMC axons ( $n = 113$ -183 hits from 3 mice). (n-o) Pre-infusing SHU9119 reduced the magnitude of POMC axon stimulation-induced cAMP increments on hit trials without affecting cAMP persistence ( $n = 9$  FOVs from 3 mice). c, j, k: mean  $\pm$  95% c.i. of hit rates; d, e, l, n, o: mean  $\pm$  s.e.m. across trials (d), hits (e, l), and FOVs (n, o). c, j: bootstrap comparison of hit rates; i: one-way ANOVA; n, o: paired t-test.



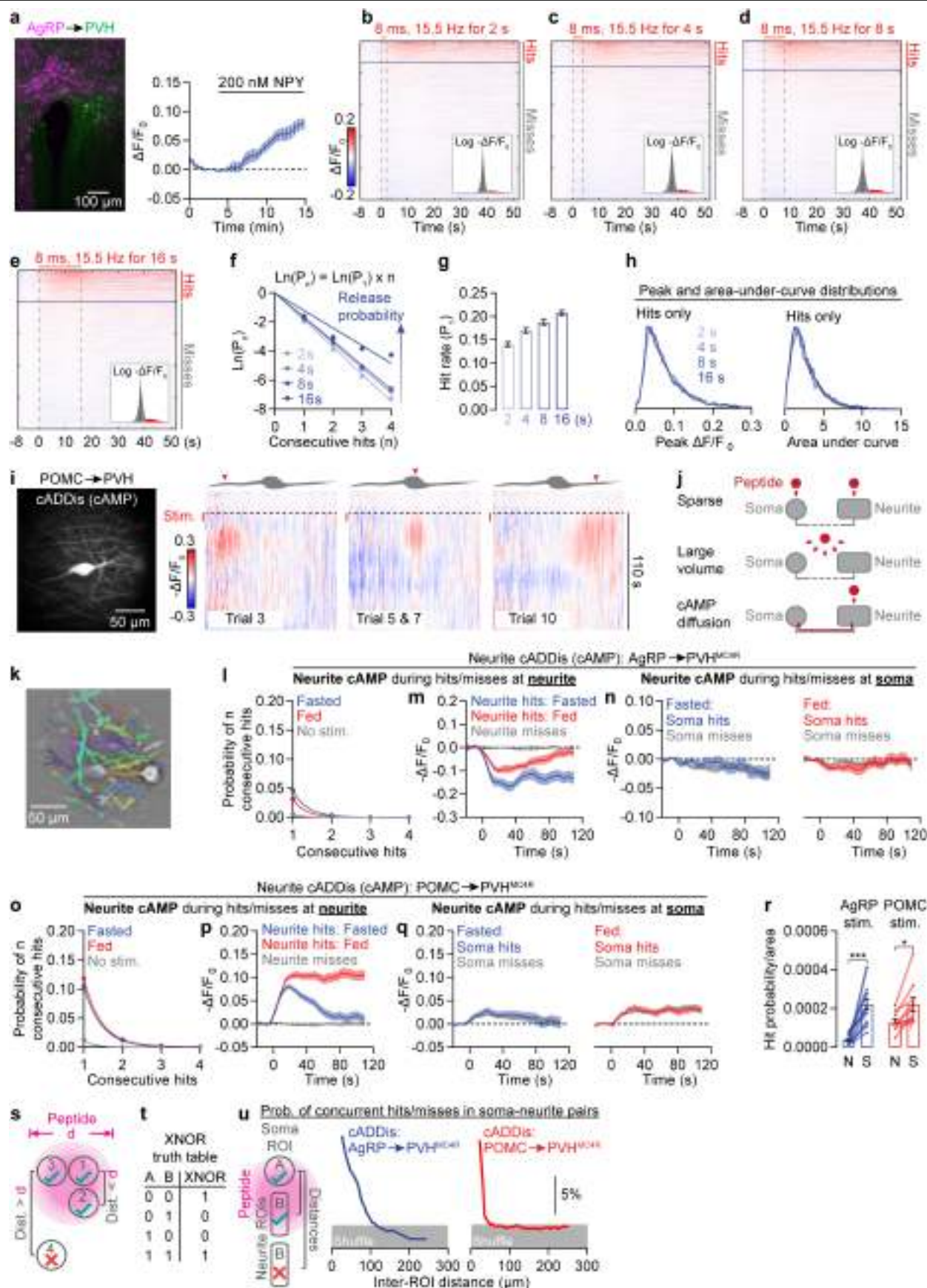
**Extended Data Fig. 3 | Characterizing NPY signalling to PVH<sup>MC4R</sup> neurons.**

(a) Mean hit rates of AgRP axon stimulation-induced cAMP decrements in PVH<sup>MC4R</sup> neurons were not different between fasted and fed states.

No-stimulation conditions in both fasted and fed states showed a low hit rate.  $n = 1093$ - $1928$  trials from 4 mice. (b) Across all trials, cAMP decrements were greater in amplitude and more persistent in the fasted state ( $n = 1190$  fasted and  $1093$  fed trials from 4 mice). No-stimulation control trials showed almost no increments or decrements. (c) cAMP decrements lasted more than 5 min in fasted mice and 1-2 min in fed mice.  $n = 262$ - $355$  hits from 4 mice. (d) Histology of cADDis expression (green) in PVH<sup>MC4R</sup> neurons and Chrimson-tdTomato expression (red) in AgRP axons. In the left panel, dotted lines delineate the GRIN lens track. In the right panel, white dotted line delineates the anterior side of the infusion cannula inserted in the lateral ventricle (LV; cyan dotted line) which contains choroid plexus (ChP). Similar histology results are obtained from all 3 mice. (e) Single-mouse fluorescence lifetime traces of cADDis in PVH<sup>MC4R</sup> neurons in response to infusion of  $0.5$  nmol NPY.  $n = 3$  mice. (f) Single field-of-view summary of decrease in cAMP in PVH<sup>MC4R</sup> neurons in response to infusion

of  $0.5$  nmol NPY ( $n = 11$  FOVs from 3 mice). Lifetime changes are averaged from the 6-9 min window. (g) Pre-infusing NPY1R antagonist BIBP3226 ( $10$  nmol) together with NPY5R antagonist CGP71683 ( $10$  nmol) reduced the hit rate of AgRP axon stimulation-induced cAMP decrements in PVH<sup>MC4R</sup> neurons ( $n = 1100$ - $1408$  trials from 3 mice). (h) Same as f but showing per-mouse data ( $n = 299$ - $568$  trials per mouse per condition). (i) Per-mouse cAMP transients during hit trials after ACSF and SHU9119 injections ( $n = 20$ - $81$  hits per mouse per condition). (j) Cumulative distribution of magnitudes of single-trial cAMP decrements (measured with cADDis) indicates a decrease in magnitudes when BIBP3226 and CGP71683 were pre-infused before optogenetic stimulations ( $n = 80$ - $208$  hits from 3 mice). (k-l) Pre-infusing BIBP3226 and CGP71683 reduced the magnitude of AgRP axon stimulation-induced cAMP decrements without affecting the persistence of these cAMP decrements ( $n = 9$  FOVs from 3 mice, paired t-test). a, g, h: mean  $\pm$  95% c.i. of hit rates; b, c, f, i, k, l: mean  $\pm$  s.e.m. across trials (b), hits (c, i) and FOVs (f, k, l). a, g: bootstrap comparison of hit rates; f: one-way ANOVA; k, l: paired t-test.



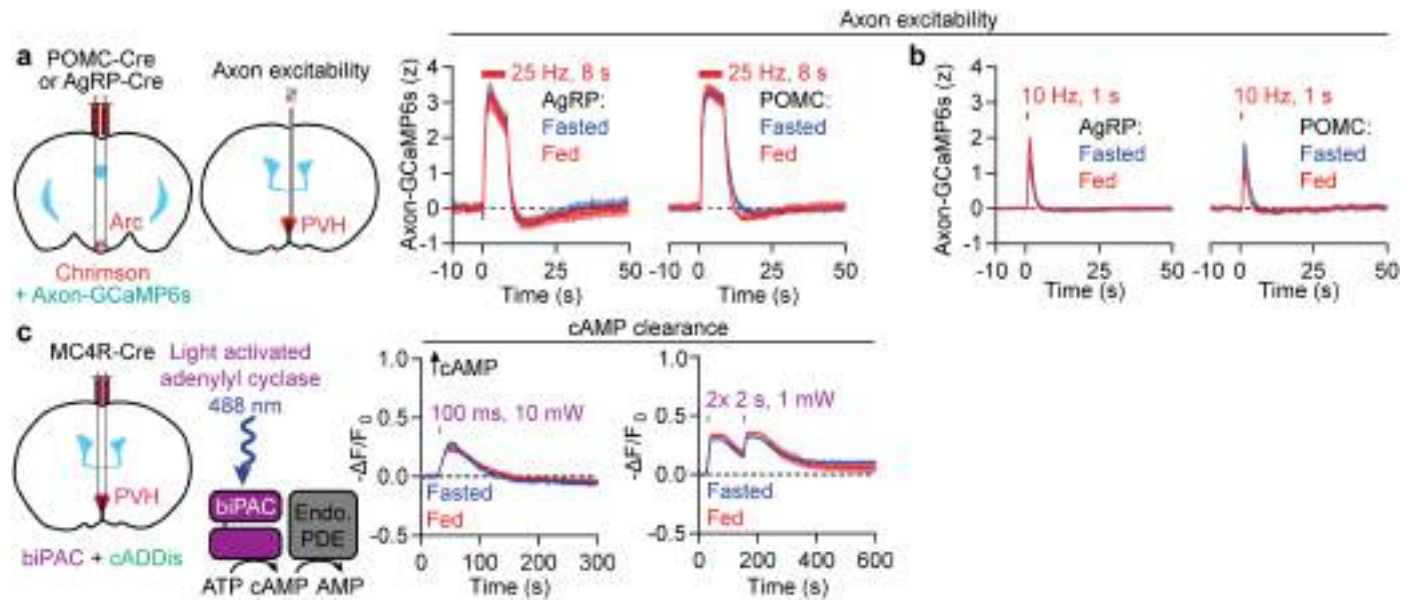


Extended Data Fig. 4 | See next page for caption.



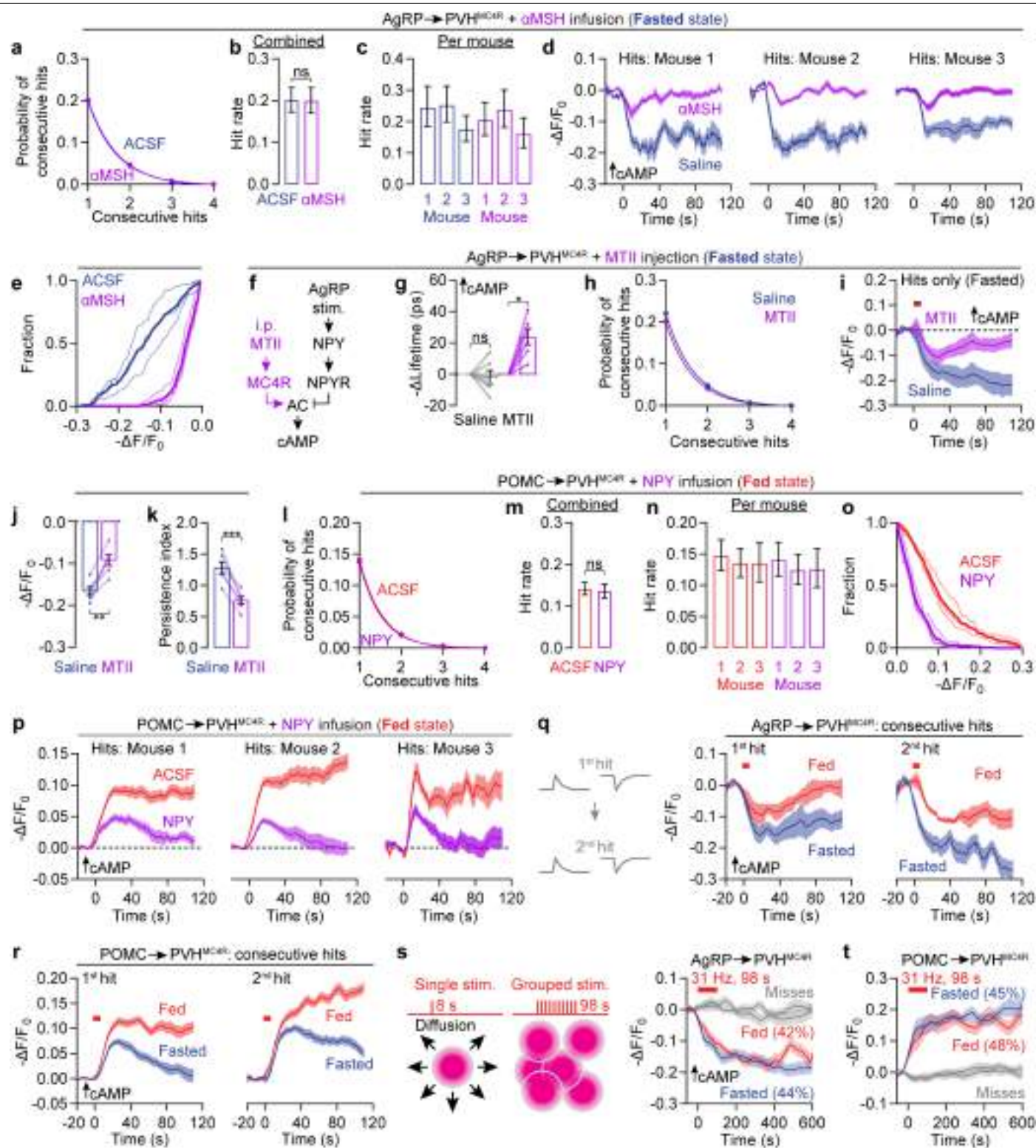
**Extended Data Fig. 4 | Stochastic neuropeptide release triggers spatially sparse cAMP signals.** (a) Left: example field view of npyLight expression in PVH (green) and Chrimson-tdTomato expression in AgRP axons (red). Right: the fluorescence of npyLight increased in response to NPY (200 nM; n = 10 slices from 4 mice). The pre-stimulation decay was likely due to photobleaching. (b-e) Summary heatmaps of single-trial npyLight signals in response to 2 s (b), 4 s (c), 8 s (d), or 16 s (e) of Chrimson photostimulation (n = 16439-19969, trials from 7 mice). Trials are sorted by peak intensity. Inset: distribution of peak intensities, colour-coded red for hits and grey for misses, with x-axis on a log scale. (f) The hit rates of AgRP axon stimulation-induced NPY signals (measured with npyLight) are mostly well described using the dice model, with a modest, sublinear increase in probability of release with increasing stimulation duration (n = 16439-19969 trials from 7 mice). (g-h) When we increased the duration of 15.5 Hz photostimulation eight-fold, from 2 s to 16 s, the hit rate of npyLight transients only increased from 14% to 21% (g: n = 16439-19969 trials from 7 mice), and hit amplitudes remained unchanged (h: n = 2632, 2782, 3736, 3595 hits). (i) In an example neuron with a clearly visible soma and two associated neurites, POMC axon stimulation-induced cAMP increments were spatially localized and occurred on different trials for the soma and for each neurite. (j) We considered three potential modes of peptide transmission. First, in the discrete model, somas and associated neurites function as independent peptide sensing compartments<sup>84,90-93</sup>, and show largely uncorrelated cAMP signalling although most neurite regions-of-interest (ROIs) connected to a soma are likely dendrites, we termed these neurites to be conservative). Second, in the large-volume transmission model<sup>1,27,94</sup>, neuropeptide signals are broadcasted widely across somas and neurites, so cAMP signals should be correlated within the same cell and across cells. Third, in the cAMP diffusion model, neuropeptide transmission is locally restricted but the resulting cAMP changes are seen in other compartments of the same cell due to intracellular diffusion. In this case, trial-by-trial cAMP signals in somas and associated neurites should be correlated. (k) Example neurite segmentation by Cellpose 2.0<sup>80</sup> nuclear model that was retrained by

manual neurite segmentation (see Methods). (l-m) Analyses of AgRP-to-PVH<sup>MC4R</sup> cAMP imaging data indicated stochastic cAMP decrements in neurites similar to those observed in somas (l). Further, neurite cAMP decrements were more persistent in the fasted state, similar to soma decrements (m). n = 6048-9371 trials from 4 mice. (n) We next evaluated the presence or absence of concurrent hits in somas and associated neurites. The neurite cAMP signals averaged across *soma* hit trials were weak and similar to signals averaged across *soma* miss trials, indicating a lack of strong correlation between a cAMP decrement in a neuron's soma and in its neurite. n = 2233 fasted and 2947 fed trials from 4 mice. (o-q) Neurite analysis of POMC-to-PVH<sup>MC4R</sup> cAMP imaging data also showed stochastic cAMP increments (o) that were more persistent in the fed state (p). Changes in neurite cAMP were weak and of similar amplitude when averaged across *soma* hit trials or miss trials, again indicating decorrelation of soma and neurite signals (q). Together with above data, these results show that neuropeptide transmission to PVH<sup>MC4R</sup> neurites largely follows the same rules as soma signalling. However, the stochastic hits and misses are decorrelated between somas and neurites of the same cell, therefore favoring the discrete compartmental model over large-volume transmission or cAMP diffusion models. (r) During both AgRP axon stimulation and POMC axon stimulation, the hit rate per area is non-zero in neurites (N) but is lower in neurites than soma (S; n = 10-13 FOVs from 8 mice). (s) Model: during spatially restricted peptide release, ROIs that are closer to each other than the impact diameter are more likely to receive the same peptide signal. (t) The truth table of exclusive not-or (XNOR), a metric of concurrence between pairs of binary events, A and B. When cAMP responses in two regions-of-interest concur on a given trial (e.g. both exhibit a hit or both exhibit a miss), the XNOR value equals one. (u) Probability of concurrent hits or misses between soma-neurite pairs drops as the distance between the two ROIs increases. The distance beyond which concurrence of cAMP responses drops to chance levels (see Methods) is ~100  $\mu$ m during both AgRP axon stimulation (left) and POMC axon stimulation (right). N = 9354-14101 trials. g: mean  $\pm$  95% c.i. of hit rates; a, m, n, p, q, r: mean  $\pm$  s.e.m. across slices (a), hits (m, n, p, q), and FOVs (r). r: one-way ANOVA.



**Extended Data Fig. 5 | State-dependent peptide signalling is not due to differences in axon excitability or cAMP degradation.** (a) To measure potential axon excitability differences across states, which could lead to differences in peptide release, we first co-expressed Chrionson<sup>95</sup> and Axon-GCaMP6s in AgRP neurons and, in separate experiments, in POMC neurons. In both cases, we implanted an optic fibre in PVH to photostimulate Chrionson-expressing axons and to record the resulting calcium transients in these same axons. Axon calcium transients evoked by 25-Hz, 8-s Chrionson stimulation in AgRP (left) and POMC axons (right) were similar in fasted and fed states ( $n = 9$  mice). (b) We then repeated the experiment using a shorter stimulation protocol. Brief 10 Hz, 1 s Chrionson stimulation of AgRP axons triggered stronger calcium transients (i.e., greater  $\Delta F/F_0$ ) in the fed state. The same photostimulation of POMC axons triggered stronger calcium transients in the fasted. These differences are presumably due to lower baseline activity (i.e., lower denominator in  $\Delta F/F_0$ ) of AgRP axons and POMC axons in the fed and fasted state, respectively. Note that these differences actually argue against a

major contribution of presynaptic excitability to the state-dependent differences in cAMP responses: AgRP axon stimulation drives weaker PVH<sup>MC4R</sup> cAMP responses in the fed state, despite the slightly stronger 1-s stimulation-evoked AgRP axon calcium signals (in  $\Delta F/F_0$ ) in the fed state. Similarly, POMC axon stimulation drives weaker PVH<sup>MC4R</sup> cAMP responses in the fasted state, despite the slightly stronger 1-s stimulation-evoked POMC axon calcium signals in the fasted state.  $n = 9$  mice. (c) To test the differential cAMP-clearance hypothesis, which has been demonstrated in the MPOA<sup>23</sup>, we compared the clearance kinetics of cAMP produced by the transient stimulation of the blue-light activated adenylyl cyclase, biPAC<sup>23,35,50</sup>. Importantly, biPAC activation bypasses endogenous peptide receptor signalling, thereby enabling a more accurate estimate of cAMP clearance rates. cAMP produced by biPAC photostimulation ( $1 \times 100$  ms or  $2 \times 2$  s) in PVH<sup>MC4R</sup> neurons was cleared by endogenous PDEs (Endo. PDEs) at similar rates in fasted and fed states, arguing against state-dependent cAMP degradation ( $n = 4$ -8 slices from 6 mice). a, b, c: mean  $\pm$  s.e.m. across mice (a, b) and slices (c).

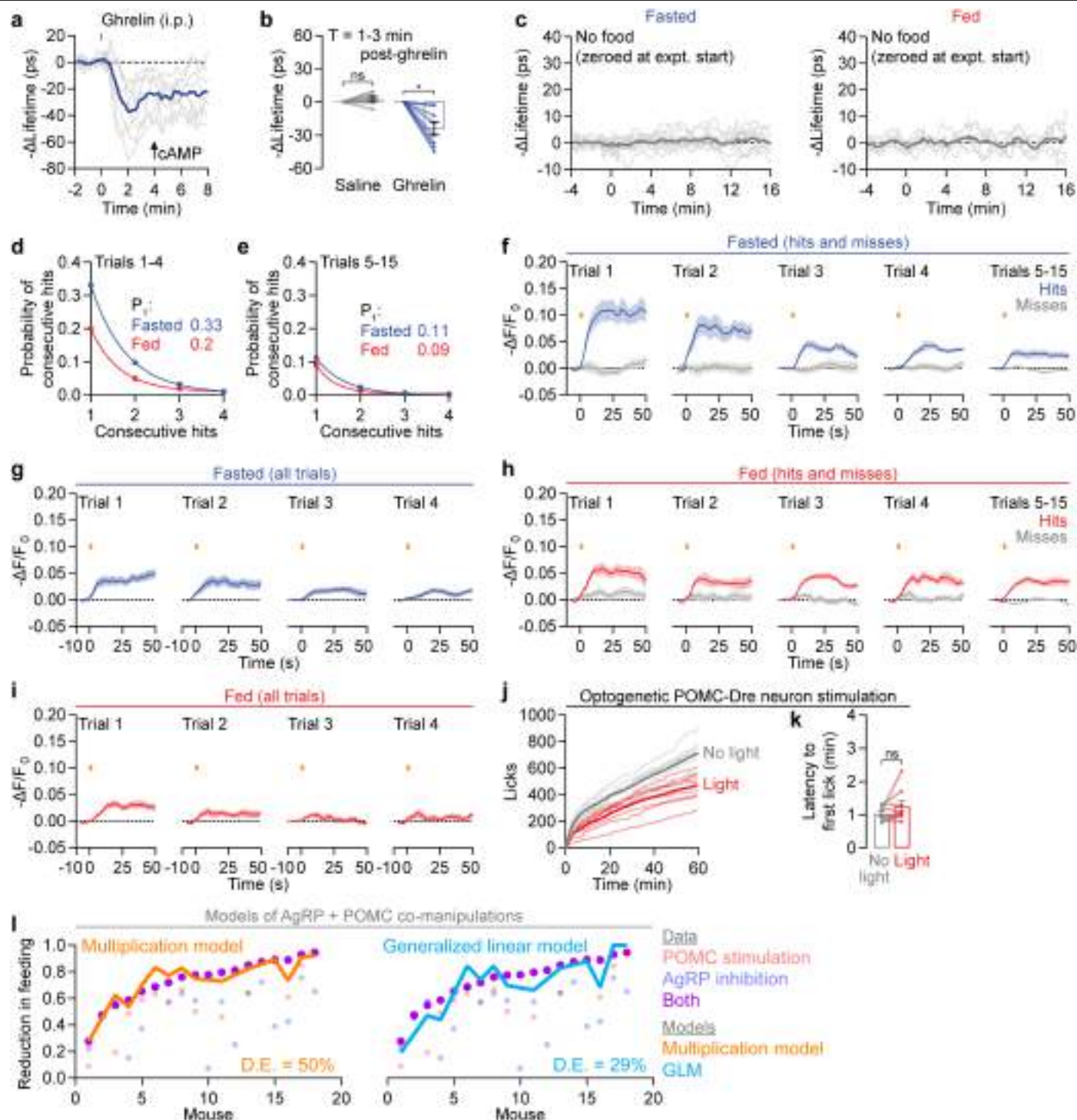


**Extended Data Fig. 6** | See next page for caption.

**Extended Data Fig. 6 | Additional evidence for the neuropeptide competition hypothesis.** (a-e)  $\alpha$ MSH pre-injection did not change the hit rate of AgRP axon stimulation-induced cAMP decrements (a-c) but reduced hit magnitudes (d-e). n = 129-145 hits from 648-722 trials and 3 mice, bootstrap comparison of hit rates. (f) MTII injection should curb AgRP axon stimulation-induced cAMP decrements. (g) MTII injection (3 mg/kg, i.p.) elevated cAMP in PVH<sup>MC4R</sup> neurons using two-photon fluorescence lifetime imaging in vivo (n = 6 FOVs from 3 mice). (h) MTII pre-injection did not change the hit rate of AgRP axon stimulation-induced cAMP decrements (n = 473-517 trials from 3 mice). (i-k) In fasted mice, pre-administration of the MC4R agonist MTII (3 mg/kg, i.p.) attenuated the amplitude and persistence of AgRP axon stimulation-induced cAMP decrements. n = 95-114 hits and 6 FOVs from 3 mice. (l-p) NPY pre-infusion did not change the hit rate of POMC axon stimulation-induced cAMP increments (l-n) but reduced hit magnitudes (o-p). n = 234-291 hits from 1701-2057 trials and 3 mice, bootstrap comparison of hit rates. (q) When analysing two consecutive hits of AgRP axon stimulation-induced cAMP decrements, the second decrement was larger than the first (n = 47-57 pairs of hits from 4 mice). Baselines were calculated separately for first and second hits to prevent lingering elevation from the first hit from contributing to the calculations of

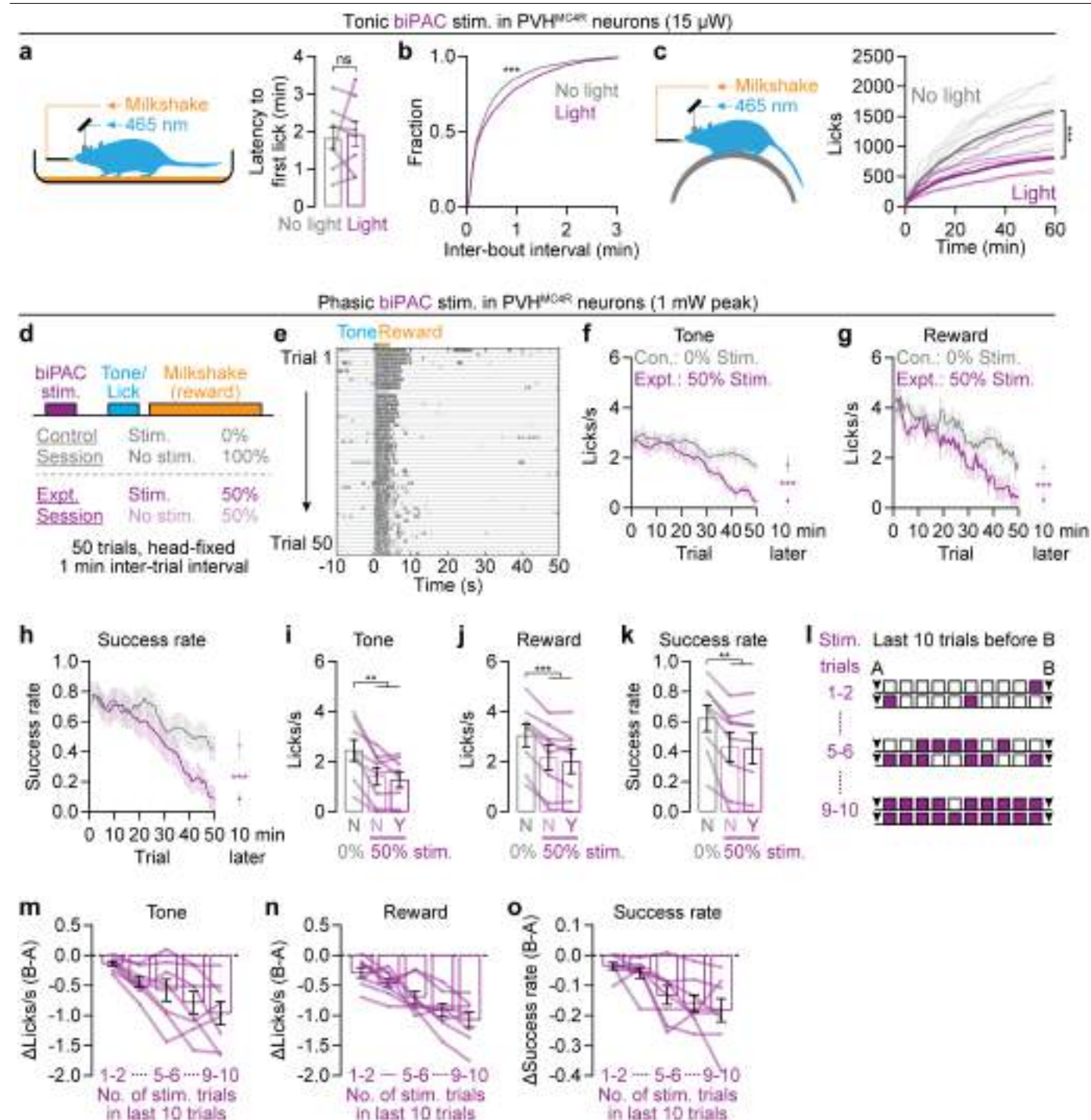
the second. (r) The same as m-o but for POMC axon stimulation-induced cAMP increments (n = 76-99 pairs of hits from 4 mice). (s-t) To more directly manipulate the total amount of peptide released in a local region of PVH, we presented groups of ten 8-s photostimulations of AgRP and POMC axons with a much shorter inter-stimulus interval (2 s instead of the 52 s used in Fig. 2; other experimental parameters were not modified). The shorter inter-stimulus intervals within each 98-s stimulation sequence should decrease the degree to which peptides released during each 8-s stimulation diffuse away or are broken down by peptidases (Xiong et al.<sup>26</sup>; Turner et al.<sup>60</sup>) between trials, resulting in greater accumulation of extracellular neuropeptide levels that could overcome endogenous competition from opposing neuropeptides (illustrated in s). Consistent with this prediction, these 98-s groups of AgRP or POMC axon stimulations drove cAMP decrements (s; 42-44% hit rate per group) and increments (t; 45-48% hit rate) that were longer-lasting (> 8 min after the last pulse) and insensitive to hunger state. s: n = 112-167 trials from 4 mice. t: n = 97-139 trials from 4 mice. d, g, i, j, k, p, q, r, s, t: mean  $\pm$  s.e.m. across FOVs (g, j, k, q, r) and hits/misses (d, i, p, s, t); b, c, m, n: mean  $\pm$  95% c.i. of hit rates. b, m: bootstrap comparison of hit rates; g: one-way ANOVA; j, k: paired t-test.





**Extended Data Fig. 7 | cAMP signalling in PVH<sup>MC4R</sup> neurons during feeding.** (a-b) Injection of ghrelin (2.5 mg/kg, i.p.), which stimulates AgRP neurons and inhibits POMC neurons, induced a robust and sustained decrease in cAMP in PVH<sup>MC4R</sup> neurons in fed mice. (c) cAMP levels were stable in PVH<sup>MC4R</sup> neurons in the absence of feeding (n = 7-11 FOVs from 3 mice), arguing against any non-stationarities due to elapsed time within a session. (d-e) cAMP increments were stochastic. The hit rate is higher in the first 4 trials (d) than the rest (e). d: n = 561-646 trials from 6 mice, e: 1542-1759 trials. (f-i) Persistent cAMP increments in the fasted (f-g) and fed states (h-i). The increments were likely caused by the increase in POMC neuron activity during feeding. This persistence likely resulted from decreased competition from NPY, due to the drop in AgRP neuron activity during feeding. f: n = 359 hits and 1744 misses from 6 mice, g: n = 561 trials, h: n = 290 hits and 2115 misses, i: n = 646 trials. g, i show only the

first four trials per session. (j-k) Optogenetic stimulation of POMC-Dre axons in the PVH suppressed food intake, and this feeding suppression was already visible in the first few minutes of the feeding assay (j). No change was seen in latency to the first lick (k). n = 9 mice. (l) On a per-mouse level, the net effect of combining simultaneous inhibition of AgRP neurons and excitation of POMC-Dre axons in the PVH can be best explained by multiplying the effect sizes of the two individual manipulations together (e.g., 50% suppression of feeding + 50% suppression of feeding = 75% suppression of feeding, orange line). This parameter-free model (zero degrees of freedom, 50% deviance explained [D.E.]) outperformed a generalized linear model (3 degrees of freedom, blue line, 29% deviance explained). b, f, g, h, i, k: mean  $\pm$  s.e.m. across FOVs (b), hits/misses (f, h), trials (g, i), and mice (k). b: one-way ANOVA; k: paired t-test.

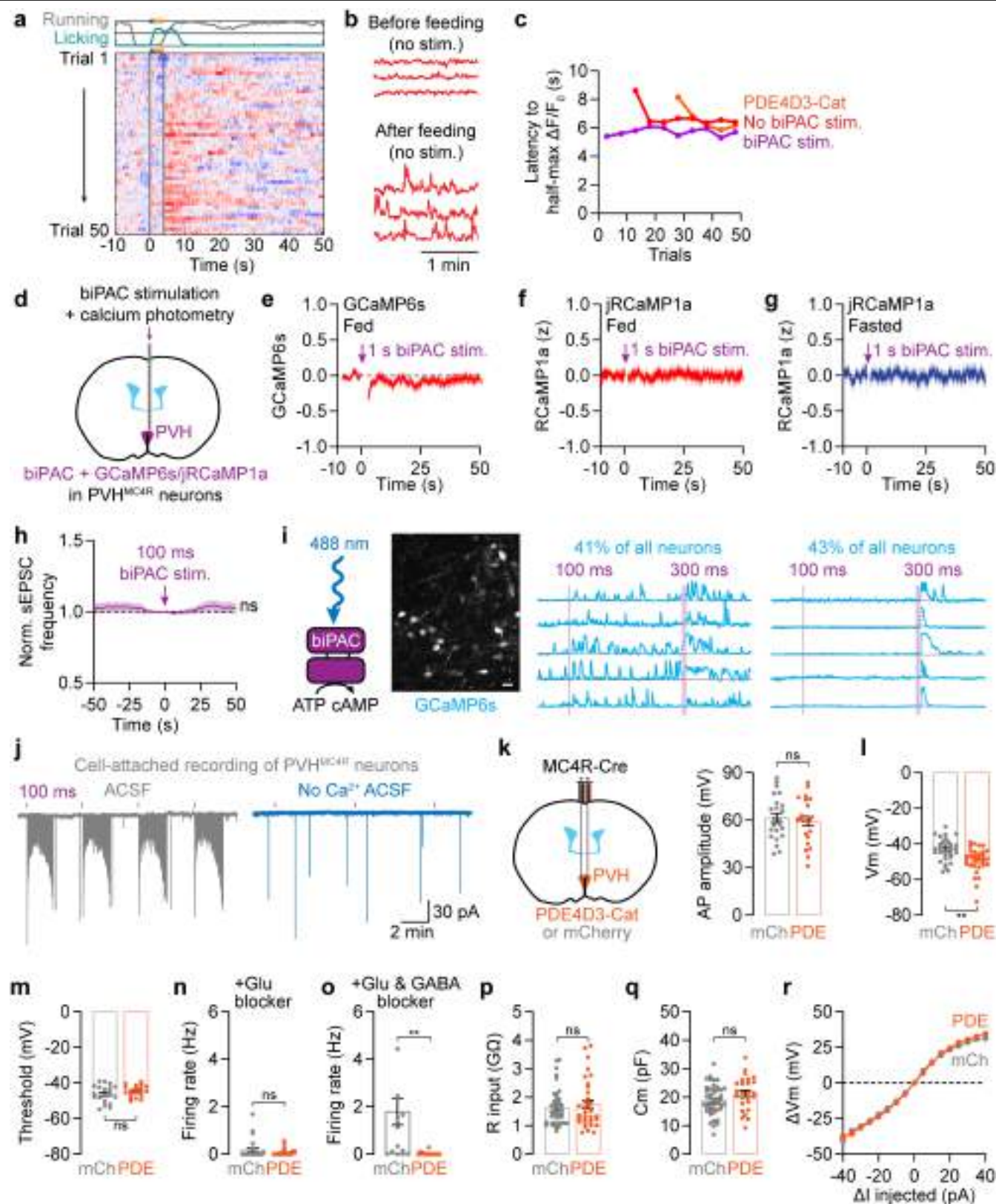


Extended Data Fig. 8 | See next page for caption.

**Extended Data Fig. 8 | Optogenetic cAMP production in PVH<sup>MC4R</sup> neurons gradually promotes satiety.** (a-b) Because freely moving mice exhibit bouts of feeding interspersed with other behaviours, we examined how the bout structure can be affected by elevated cAMP production. Tonic weak biPAC stimulation (15  $\mu$ W) increased inter-bout interval (b), but did not affect latency to first lick (a). Stimulation started when a lick spout was placed inside the cage. We define the termination of a bout as the lack of licking for 5 seconds.  $n = 8$  mice. (c) Continuous photostimulation of cAMP production (biPAC, -15  $\mu$ W) in PVH<sup>MC4R</sup> neurons reduced cumulative lick rate in fasted, head-fixed mice. Food source and lickspout design were kept the same as a-b.  $n = 8$  mice. (d) To understand the timescale of the satiety-promoting effect of biPAC stimulation, we designed a task in which mice lick during an audible cue ("Tone") to obtain milkshake ("Reward"). The purpose of the cue was to synchronize consumption and allow for trial-locked optogenetic stimulation of cAMP production in some trials. We used one of two types of sessions on alternating days, with each session containing 50 trials at 1 trial/min. In control sessions, no biPAC stimulation was delivered. In experimental sessions, biPAC stimulation was delivered on a random 50% of trials and consisted of 1 s of stimulation starting 5 s before cue onset. This randomized biPAC stimulation design allowed for within-session behavioural analysis, and the 5-s delay between stimulation and cue onset allowed for cAMP to reach peak levels during cue and reward delivery

(see Extended Data Fig. 5c). (e) In an assay where fasted mice licked during a tone (blue) to obtain reward (orange, milkshake), well-trained food-restricted mice started licking during the tone but the lick rate gradually decreased over 50 trials. (f-h) In experimental sessions (purple) in which biPAC stimulation was delivered in 50% of the trials, lick rates during tone (f), following reward delivery (g), and success rates (i.e., rate at which the mouse exhibited licking following the tone but prior to the reward delivery; h) drop off faster than in control sessions (grey). The lick rates and success rates did not recover after an additional 10 min with no biPAC stimulation, indicating satiety rather than transient disengagement.  $n = 8$  mice. (i-k) Within the experimental session, no difference in lick rate during tone (i), lick rate following reward delivery (j), or success rate (k) was observed between stimulation trials (purple, 'Y') and no-stimulation trials (purple, 'N'). These results show that elevation of cAMP does not drive an immediate change in behaviour.  $n = 8$  mice. (l-o) Over a window of 10 trials (l), the decrease in lick rate during tone (m), following reward delivery (n), and success rate of correct licking following the cue (o) scaled with the total number of biPAC stimulations delivered across the last ten trials ( $n = 8$  mice). Together with panels i-k, this suggests that the feeding-suppressing effects of cAMP increments are gradual (i.e., they do not affect same-trial performance) and cumulative across minutes. a, f, g, h, i, j, k, m, n, o: mean  $\pm$  s.e.m. across mice. a, c, f, g, h: paired t-test; b: Kolmogorov-Smirnov test; i, j, k: one-way ANOVA.





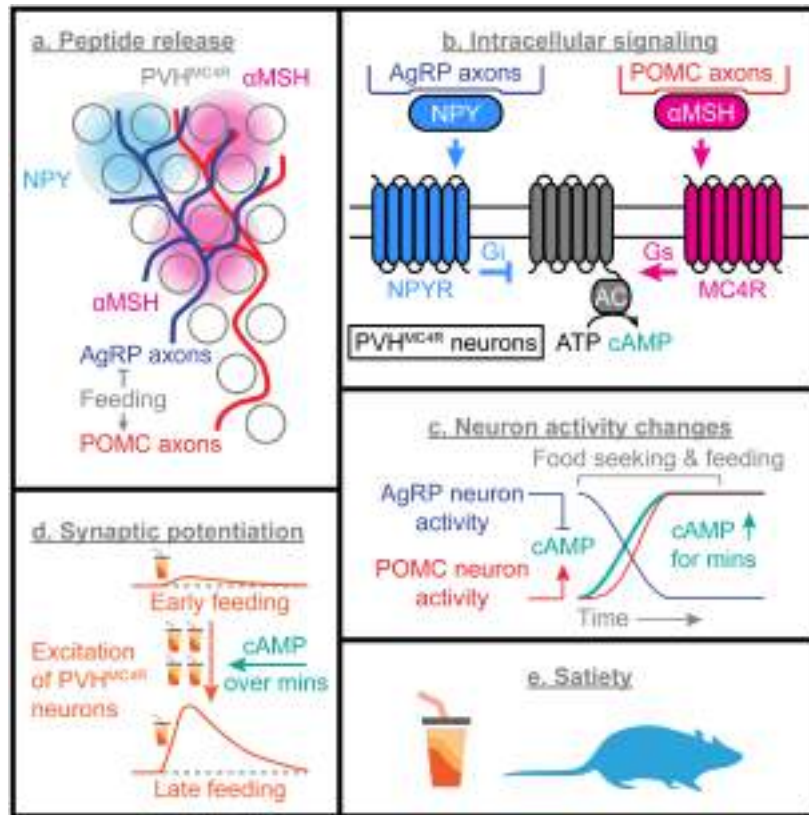
Extended Data Fig. 9 | See next page for caption.



**Extended Data Fig. 9 | cAMP potentiates excitatory inputs to PVH<sup>MC4R</sup>**

**neurons.** (a) An example session from a fasted mouse that licks during the cue (blue square above heatmap) to obtain reward (orange rectangle above heatmap). The panel shows a heatmap of jRCaMP1a photometry signals (each row is a trial). There was a delayed increase in calcium activity during each trial (which peaks ~4 s after cue onset, and several seconds after consumption onset), potentially reflecting ingestion-related gastrointestinal signals. This increase in activity took ~10 trials to develop. (b) Photometry recording of spontaneous bulk calcium activity after a session suggests increases in ongoing PVH<sup>MC4R</sup> calcium activity after feeding. (c) cAMP manipulations by biPAC or PDE4D3-Cat did not significantly change the timing of PVH<sup>MC4R</sup> neurons' activation. The latency was defined as time between cue onset and the half-max point in the rising phase of the  $\Delta F/F_0$  trace.  $n = 8$  mice per condition. (d-g) In mice co-expressing biPAC and a calcium sensor (GCaMP6s or RCaMP1a) in PVH<sup>MC4R</sup> neurons (d), briefly stimulating biPAC through a fibre did not result in noticeable calcium transients in either fed mice (e and f) or fasted mice (g). We tested jRCaMP1a, a green-light sensitive calcium sensor, to avoid biPAC activation by photometry light. Blanking (2-4 s) in traces was done to remove temporary photobleaching due to optogenetic stimulation.  $n = 8$  mice per panel. (h) Brief 100-ms biPAC stimulation did not increase the frequency of spontaneous excitatory inputs, thereby sensitizing PVH<sup>MC4R</sup> neurons to excitatory inputs.  $n = 26$  cells from 5 fed mice. (i) In acute brain slices, brief biPAC activation (100 ms or 300 ms, 10 mW) resulted in changes in calcium activity that can be described using two main categories: 41% of PVH<sup>MC4R</sup>

neurons showed a persistent elevation in calcium activity, while a different 43% showed relatively transient (~100 s) increases in calcium activity ( $n = 5$  slices from 2 fed mice). Because the transient activation was not seen in vivo (see Extended Data Fig. 9d-g), we did not pursue it further. (j) Example cell-attached recording shows elevated firing rate (negative deflections) for ~2 min after each brief biPAC stimulation pulse (100 ms). The acute neuronal activation by biPAC stimulation was not seen in vivo (see Extended Data Fig. 9d-g). Such a difference between slice and in vivo results could be due to lower extracellular calcium concentration in vivo, as the excitability effects in slice depended on extracellular calcium (right). (k-m) In PVH<sup>MC4R</sup> neurons in brain slices from fed mice, cAMP degradation by PDE4D3-Cat (3-4 weeks post-injection) did not affect action potential amplitudes (k) or spike threshold membrane potential (m), but did hyperpolarize these neurons (l). k:  $n = 23$  cells from 6 mice, l:  $n = 31-32$  cells from 6 mice, m:  $n = 19-20$  cells from 6 mice. mCh: mCherry control. (n-o) In slices containing the glutamate blocker kynurenic acid (1 mM; n), PVH<sup>MC4R</sup> neurons from fed mice ceased spontaneous firing ( $n = 25$  cells from 4 fed mice). Adding the GABA blocker Gabazine (20  $\mu$ M; o) rescued some spontaneous firing in a subset of control cells but not in PDE4D3-Cat-expressing cells ( $n = 16$  cells from 4 fed mice). These results demonstrate the role of synaptic inputs in regulating the spontaneous spiking patterns of PVH<sup>MC4R</sup> neurons. (p-r) PDE4D3-Cat expression did not change input resistance (p), membrane capacitance (q), or the I-V relation (r) of PVH<sup>MC4R</sup> neurons. p: 33-43 cells from 6 mice, q: 26-45 cells from 6 mice, r: 24-26 cells from 6 mice. e, f, g, h, k, l, m, n, o, p, q, r: mean  $\pm$  s.e.m. across mice (e, f, g) and cells (h, k, l, m, n, o, p, q, r). n, o, p, q: unpaired t-test.



**Extended Data Fig. 10 | Summary of findings.** We have used imaging and manipulation of cAMP signalling to investigate spatiotemporal neuropeptide dynamics and downstream biochemical computations. These computations gradually culminate in changes in PVH<sup>MC4R</sup> neuron spiking activity that only then become detectable using conventional calcium imaging and electrophysiology. We show that photostimulation of the neuropeptide-releasing axons of AgRP and POMC neurons leads to stochastic neuropeptide release (a). This stochasticity, together with restricted peptide diffusion, enables a temporally and spatially sparse mode of signalling, in which stochastic cAMP transients are detected in subcellular compartments of downstream PVH<sup>MC4R</sup> neurons.

In addition to having opposite effects on cAMP production, hunger and satiety peptides also inhibit each other's signalling efficacy, rendering NPY signalling dominant in the fasted state and αMSH signalling dominant in the fed state (b). Feeding resolves this competition between peptides by simultaneously increasing αMSH release and decreasing NPY release, resulting in a gradual accumulation of cAMP in PVH<sup>MC4R</sup> neurons (c). Finally, cAMP gradually sensitizes PVH<sup>MC4R</sup> neurons to feeding-related excitatory inputs (d), thereby calibrating the gradual activation of these satiety-promoting neurons to the accumulation of a sufficient amount of food (e).

## Reporting Summary

Nature Research wishes to improve the reproducibility of the work that we publish. This form provides structure for consistency and transparency in reporting. For further information on Nature Research policies, see our [Editorial Policies](#) and the [Editorial Policy Checklist](#).

### Statistics

For all statistical analyses, confirm that the following items are present in the figure legend, table legend, main text, or Methods section.

n/a Confirmed

- ☐ ☒ The exact sample size ( $n$ ) for each experimental group/condition, given as a discrete number and unit of measurement
- ☐ ☒ A statement on whether measurements were taken from distinct samples or whether the same sample was measured repeatedly
- ☐ ☒ The statistical test(s) used AND whether they are one- or two-sided  
*Only common tests should be described solely by name; describe more complex techniques in the Methods section.*
- ☐ ☒ A description of all covariates tested
- ☐ ☒ A description of any assumptions or corrections, such as tests of normality and adjustment for multiple comparisons
- ☐ ☒ A full description of the statistical parameters including central tendency (e.g. means) or other basic estimates (e.g. regression coefficient) AND variation (e.g. standard deviation) or associated estimates of uncertainty (e.g. confidence intervals)
- ☐ ☒ For null hypothesis testing, the test statistic (e.g.  $F$ ,  $t$ ,  $r$ ) with confidence intervals, effect sizes, degrees of freedom and  $P$  value noted  
*Give  $P$  values as exact values whenever suitable.*
- ☒ ☐ For Bayesian analysis, information on the choice of priors and Markov chain Monte Carlo settings
- ☒ ☐ For hierarchical and complex designs, identification of the appropriate level for tests and full reporting of outcomes
- ☐ ☒ Estimates of effect sizes (e.g. Cohen's  $d$ , Pearson's  $r$ ), indicating how they were calculated

*Our web collection on [statistics for biologists](#) contains articles on many of the points above.*

### Software and code

Policy information about [availability of computer code](#)

- |                 |   |
|-----------------|---|
| Data collection | Standard two-photon imaging data were collected with Scanbox implemented in Matlab 2020 (NeuroLabWare). Two-photon FLIM data were collected with SPCM (Becker & Hickl). Photometry data were collected in Matlab 2021   |
| Data analysis   | Data analysis was performed in Matlab 2021, Prism 9, Python 3.8, ImageJ 1.51f, and SPCImage 8.0. All analysis scripts and functions are available online at <a href="https://github.com/xzhang03/Code-for-Zhang-and-Kim-et-al">https://github.com/xzhang03/Code-for-Zhang-and-Kim-et-al</a> |

For manuscripts utilizing custom algorithms or software that are central to the research but not yet described in published literature, software must be made available to editors and reviewers. We strongly encourage code deposition in a community repository (e.g. GitHub). See the Nature Research [guidelines for submitting code & software](#) for further information.

### Data

Policy information about [availability of data](#)

All manuscripts must include a [data availability statement](#). This statement should provide the following information, where applicable:

- Accession codes, unique identifiers, or web links for publicly available datasets
- A list of figures that have associated raw data
- A description of any restrictions on data availability

Figure source data are available as spreadsheets that accompany this manuscript. Raw two-photon imaging and two-photon fluorescence imaging datasets are available from the corresponding authors upon request.

# Field-specific reporting

Please select the one below that is the best fit for your research. If you are not sure, read the appropriate sections before making your selection.

☒ Life sciences

☐ Behavioural & social sciences

☐ Ecological, evolutionary & environmental sciences

For a reference copy of the document with all sections, see [nature.com/documents/nr-reporting-summary-flat.pdf](https://www.nature.com/documents/nr-reporting-summary-flat.pdf)

## Life sciences study design

All studies must disclose on these points even when the disclosure is negative.

Sample size	No statistical methods were used to pre-determine sample sizes, but our sample sizes were chosen to reliably measure experimental parameters and keep with standards of the relevant fields [Refs 11,23,36,40,47,61–64], while remaining in compliance with ethical guidelines to minimize the number of experimental animals.
Data exclusions	Data were only excluded if post-hoc histological verification showed that either viral infection or GRIN/fiber implantation missed the target region.
Replication	For most experiments, each mouse was considered an independent replicate (typically as a mean of 2-3 trials). For two-photon imaging experiments, each field of view was considered a replicate. For slice imaging experiments, each slice was considered a replicate. For comparisons of fractions, we calculated the fractions by pooling the trials of the same condition while keeping the trials from each animal equal (typically 2-3). For all other types of experiments, each mouse was a replicate. For each panel where a representative image is shown, similar independent images from different mice were reproduced at least 3 times. All behavioral assays and recordings were conducted in 2-3 independent batches per experiment, and only results that are consistent between batches are used in the paper. In addition, whenever appropriate, we tested the same hypothesis with different experimental settings. For example, we used food-intake data both in home cages and in metabolic chambers to confirm PDE4D3-Cat-induced obesity.
Randomization	Randomization was used whenever possible to determine experimental order and group assignments. The list of experiments is as follows: 1. expression of PDE4D3-Cat or mCherry among littermates for energy-balance experiments, 2) optogenetic Chrimson stimulation or no stimulation in an imaging session, 3) infusing/injecting neuropeptide drugs or vehicle in any imaging session, 3) optogenetic biPAC stimulation or no stimulation in an imaging or photometry session, 4) 50% or 0% trials with biPAC stimulation in a behavioral session, 5) AgRP inhibition, or POMC stimulation, or neither, or both in any feeding-behavioral session, 6) expression of calcium sensor + biPAC or calcium sensor + PDE4D3-Cat among littermates for photometry experiments. The only non-randomized experiments are hunger-state-dependent cAMP or axon-excitability measurements (to avoid unnecessarily frequent fasting-refeeding cycles, the order is always 50% of fed state experiments, all fasted state experiments, and the remaining 50% of the fed state experiments), 2) biPAC electrophysiology experiments (all mice were injected with biPAC and stimulation was delivered on all trials).
Blinding	Experimenters were not blinded. No prior assumptions were made on the selection of animals, experimental order, images, etc. Whenever possible, we invested time to develop automated data analysis tools for food intake, image registration, soma, and neurite segmentation (using existing tool Cellpose2.0), cAMP transient classification, NPY release, spatial analyses of cAMP and NPY signals, cAMP sensor FLIM quantification, calcium photometry, and electrophysiology data. All analysis packages are open-source and can be found at <a href="https://github.com/xzhang03/Code-for-Zhang-and-Kim-et-al">https://github.com/xzhang03/Code-for-Zhang-and-Kim-et-al</a>

## Behavioural & social sciences study design

All studies must disclose on these points even when the disclosure is negative.

Study description	Briefly describe the study type including whether data are quantitative, qualitative, or mixed-methods (e.g. qualitative cross-sectional, quantitative experimental, mixed-methods case study).
Research sample	State the research sample (e.g. Harvard university undergraduates, villagers in rural India) and provide relevant demographic information (e.g. age, sex) and indicate whether the sample is representative. Provide a rationale for the study sample chosen. For studies involving existing datasets, please describe the dataset and source.
Sampling strategy	Describe the sampling procedure (e.g. random, snowball, stratified, convenience). Describe the statistical methods that were used to predetermine sample size OR if no sample-size calculation was performed, describe how sample sizes were chosen and provide a rationale for why these sample sizes are sufficient. For qualitative data, please indicate whether data saturation was considered, and what criteria were used to decide that no further sampling was needed.
Data collection	Provide details about the data collection procedure, including the instruments or devices used to record the data (e.g. pen and paper, computer, eye tracker, video or audio equipment) whether anyone was present besides the participant(s) and the researcher, and whether the researcher was blind to experimental condition and/or the study hypothesis during data collection.
Timing	Indicate the start and stop dates of data collection. If there is a gap between collection periods, state the dates for each sample cohort.
Data exclusions	If no data were excluded from the analyses, state so OR if data were excluded, provide the exact number of exclusions and the rationale behind them, indicating whether exclusion criteria were pre-established.



Non-participation

State how many participants dropped out/declined participation and the reason(s) given OR provide response rate OR state that no participants dropped out/declined participation.

Randomization

If participants were not allocated into experimental groups, state so OR describe how participants were allocated to groups, and if allocation was not random, describe how covariates were controlled.

## Ecological, evolutionary & environmental sciences study design

All studies must disclose on these points even when the disclosure is negative.

Study description

Briefly describe the study. For quantitative data include treatment factors and interactions, design structure (e.g. factorial, nested, hierarchical), nature and number of experimental units and replicates.

Research sample

Describe the research sample (e.g. a group of tagged *Passer domesticus*, all *Stenocereus thurberi* within Organ Pipe Cactus National Monument), and provide a rationale for the sample choice. When relevant, describe the organism taxa, source, sex, age range and any manipulations. State what population the sample is meant to represent when applicable. For studies involving existing datasets, describe the data and its source.

Sampling strategy

Note the sampling procedure. Describe the statistical methods that were used to predetermine sample size OR if no sample-size calculation was performed, describe how sample sizes were chosen and provide a rationale for why these sample sizes are sufficient.

Data collection

Describe the data collection procedure, including who recorded the data and how.

Timing and spatial scale

Indicate the start and stop dates of data collection, noting the frequency and periodicity of sampling and providing a rationale for these choices. If there is a gap between collection periods, state the dates for each sample cohort. Specify the spatial scale from which the data are taken

Data exclusions

If no data were excluded from the analyses, state so OR if data were excluded, describe the exclusions and the rationale behind them, indicating whether exclusion criteria were pre-established.

Reproducibility

Describe the measures taken to verify the reproducibility of experimental findings. For each experiment, note whether any attempts to repeat the experiment failed OR state that all attempts to repeat the experiment were successful.

Randomization

Describe how samples/organisms/participants were allocated into groups. If allocation was not random, describe how covariates were controlled. If this is not relevant to your study, explain why.

Blinding

Describe the extent of blinding used during data acquisition and analysis. If blinding was not possible, describe why OR explain why blinding was not relevant to your study.

Did the study involve field work? ☐ Yes ☐ No

## Field work, collection and transport

Field conditions

Describe the study conditions for field work, providing relevant parameters (e.g. temperature, rainfall).

Location

State the location of the sampling or experiment, providing relevant parameters (e.g. latitude and longitude, elevation, water depth).

Access &amp; import/export

Describe the efforts you have made to access habitats and to collect and import/export your samples in a responsible manner and in compliance with local, national and international laws, noting any permits that were obtained (give the name of the issuing authority, the date of issue, and any identifying information).

Disturbance

Describe any disturbance caused by the study and how it was minimized.

## Reporting for specific materials, systems and methods

We require information from authors about some types of materials, experimental systems and methods used in many studies. Here, indicate whether each material, system or method listed is relevant to your study. If you are not sure if a list item applies to your research, read the appropriate section before selecting a response.

## Materials &amp; experimental systems

n/a	Involved in the study
<input type="checkbox"/>	<input checked="" type="checkbox"/> Antibodies
<input checked="" type="checkbox"/>	<input type="checkbox"/> Eukaryotic cell lines
<input checked="" type="checkbox"/>	<input type="checkbox"/> Palaeontology and archaeology
<input type="checkbox"/>	<input checked="" type="checkbox"/> Animals and other organisms
<input checked="" type="checkbox"/>	<input type="checkbox"/> Human research participants
<input checked="" type="checkbox"/>	<input type="checkbox"/> Clinical data
<input checked="" type="checkbox"/>	<input type="checkbox"/> Dual use research of concern

## Methods

n/a	Involved in the study
<input checked="" type="checkbox"/>	<input type="checkbox"/> ChIP-seq
<input checked="" type="checkbox"/>	<input type="checkbox"/> Flow cytometry
<input checked="" type="checkbox"/>	<input type="checkbox"/> MRI-based neuroimaging

## Antibodies

Antibodies used	The primary antibodies used in this paper are chicken anti-GFP (1:1000, Invitrogen; used for GFP and GCaMP6s) and rat anti-mCherry (1:1000, ThermoFisher; used for mCherry and tdTomato). The secondary antibodies are Donkey anti-chicken 488 (1:1000, Jackson) and Donkey anti-rat 594 (1:1000, Jackson).
Validation	The GFP and mCherry antibodies were previously confirmed in the lab (e.g., Livneh et al., 2017; Lutas et al., 2019; Zhang et al., 2021).

## Eukaryotic cell lines

Policy information about [cell lines](#)

Cell line source(s)	State the source of each cell line used.
Authentication	Describe the authentication procedures for each cell line used OR declare that none of the cell lines used were authenticated.
Mycoplasma contamination	Confirm that all cell lines tested negative for mycoplasma contamination OR describe the results of the testing for mycoplasma contamination OR declare that the cell lines were not tested for mycoplasma contamination.
Commonly misidentified lines (See <a href="#">ICLAC</a> register)	Name any commonly misidentified cell lines used in the study and provide a rationale for their use.

## Palaeontology and Archaeology

Specimen provenance	Provide provenance information for specimens and describe permits that were obtained for the work (including the name of the issuing authority, the date of issue, and any identifying information).
Specimen deposition	Indicate where the specimens have been deposited to permit free access by other researchers.
Dating methods	If new dates are provided, describe how they were obtained (e.g. collection, storage, sample pretreatment and measurement), where they were obtained (i.e. lab name), the calibration program and the protocol for quality assurance OR state that no new dates are provided.
<input type="checkbox"/> Tick this box to confirm that the raw and calibrated dates are available in the paper or in Supplementary Information.	
Ethics oversight	Identify the organization(s) that approved or provided guidance on the study protocol, OR state that no ethical approval or guidance was required and explain why not.

Note that full information on the approval of the study protocol must also be provided in the manuscript.

## Animals and other organisms

Policy information about [studies involving animals](#); [ARRIVE guidelines](#) recommended for reporting animal research

Laboratory animals	Male and female mice older than 8 weeks were used in experiments, and the numbers of males and females were balanced to the degree allowed by each litter (see Supplementary Table 1). Sex-specific analyses show consistent effects in males and females, but male mice were typically larger in size and ate more (Supplementary Table 1). We used the following genotypes: B6.FVB-Tg(Pomc-cre)1Low/J (POMC-Cre, 010714, The Jackson Laboratory), POMC-Dre, Agrptm1(cre)Low/J (AgRP-IRES-Cre, 012899, The Jackson Laboratory), Mc4rtm3.1(cre)Low/J (MC4R-2A-Cre4, 030759, The Jackson Laboratory), and their F1 progeny.
Wild animals	The study did not involve wild animals.
Field-collected samples	The study did not involve field-collected samples.
Ethics oversight	All animal care and experimental procedures were approved by the Institutional Animal Care and Use Committee at Beth Israel Deaconess Medical Center.

Note that full information on the approval of the study protocol must also be provided in the manuscript.

## Human research participants

Policy information about [studies involving human research participants](#)

### Population characteristics

*Describe the covariate-relevant population characteristics of the human research participants (e.g. age, gender, genotypic information, past and current diagnosis and treatment categories). If you filled out the behavioural & social sciences study design questions and have nothing to add here, write "See above."*

### Recruitment

*Describe how participants were recruited. Outline any potential self-selection bias or other biases that may be present and how these are likely to impact results.*

### Ethics oversight

*Identify the organization(s) that approved the study protocol.*

Note that full information on the approval of the study protocol must also be provided in the manuscript.

## Clinical data

Policy information about [clinical studies](#)

All manuscripts should comply with the ICMJE [guidelines for publication of clinical research](#) and a completed [CONSORT checklist](#) must be included with all submissions.

### Clinical trial registration

*Provide the trial registration number from ClinicalTrials.gov or an equivalent agency.*

### Study protocol

*Note where the full trial protocol can be accessed OR if not available, explain why.*

### Data collection

*Describe the settings and locales of data collection, noting the time periods of recruitment and data collection.*

### Outcomes

*Describe how you pre-defined primary and secondary outcome measures and how you assessed these measures.*

## Dual use research of concern

Policy information about [dual use research of concern](#)

### Hazards

Could the accidental, deliberate or reckless misuse of agents or technologies generated in the work, or the application of information presented in the manuscript, pose a threat to:

- | No                       | Yes   |
|--------------------------|---|
| <input type="checkbox"/> | <input type="checkbox"/> Public health              |
| <input type="checkbox"/> | <input type="checkbox"/> National security          |
| <input type="checkbox"/> | <input type="checkbox"/> Crops and/or livestock     |
| <input type="checkbox"/> | <input type="checkbox"/> Ecosystems                 |
| <input type="checkbox"/> | <input type="checkbox"/> Any other significant area |

### Experiments of concern

Does the work involve any of these experiments of concern:

- | No                       | Yes  |
|--------------------------|--|
| <input type="checkbox"/> | <input type="checkbox"/> Demonstrate how to render a vaccine ineffective                             |
| <input type="checkbox"/> | <input type="checkbox"/> Confer resistance to therapeutically useful antibiotics or antiviral agents |
| <input type="checkbox"/> | <input type="checkbox"/> Enhance the virulence of a pathogen or render a nonpathogen virulent        |
| <input type="checkbox"/> | <input type="checkbox"/> Increase transmissibility of a pathogen                                     |
| <input type="checkbox"/> | <input type="checkbox"/> Alter the host range of a pathogen  |
| <input type="checkbox"/> | <input type="checkbox"/> Enable evasion of diagnostic/detection modalities                           |
| <input type="checkbox"/> | <input type="checkbox"/> Enable the weaponization of a biological agent or toxin                     |
| <input type="checkbox"/> | <input type="checkbox"/> Any other potentially harmful combination of experiments and agents         |

## ChIP-seq

### Data deposition

- ☐ Confirm that both raw and final processed data have been deposited in a public database such as [GEO](#).
- ☐ Confirm that you have deposited or provided access to graph files (e.g. BED files) for the called peaks.

**Data access links**

May remain private before publication.

For "Initial submission" or "Revised version" documents, provide reviewer access links. For your "Final submission" document, provide a link to the deposited data.

**Files in database submission**

Provide a list of all files available in the database submission.

**Genome browser session**(e.g. [UCSC](#))

Provide a link to an anonymized genome browser session for "Initial submission" and "Revised version" documents only, to enable peer review. Write "no longer applicable" for "Final submission" documents.

## Methodology

**Replicates**

Describe the experimental replicates, specifying number, type and replicate agreement.

**Sequencing depth**

Describe the sequencing depth for each experiment, providing the total number of reads, uniquely mapped reads, length of reads and whether they were paired- or single-end.

**Antibodies**

Describe the antibodies used for the ChIP-seq experiments; as applicable, provide supplier name, catalog number, clone name, and lot number.

**Peak calling parameters**

Specify the command line program and parameters used for read mapping and peak calling, including the ChIP, control and index files used.

**Data quality**

Describe the methods used to ensure data quality in full detail, including how many peaks are at FDR 5% and above 5-fold enrichment.

**Software**

Describe the software used to collect and analyze the ChIP-seq data. For custom code that has been deposited into a community repository, provide accession details.

## Flow Cytometry

### Plots

Confirm that:

- ☐ The axis labels state the marker and fluorochrome used (e.g. CD4-FITC).
- ☐ The axis scales are clearly visible. Include numbers along axes only for bottom left plot of group (a 'group' is an analysis of identical markers).
- ☐ All plots are contour plots with outliers or pseudocolor plots.
- ☐ A numerical value for number of cells or percentage (with statistics) is provided.

### Methodology

**Sample preparation**

Describe the sample preparation, detailing the biological source of the cells and any tissue processing steps used.

**Instrument**

Identify the instrument used for data collection, specifying make and model number.

**Software**

Describe the software used to collect and analyze the flow cytometry data. For custom code that has been deposited into a community repository, provide accession details.

**Cell population abundance**

Describe the abundance of the relevant cell populations within post-sort fractions, providing details on the purity of the samples and how it was determined.

**Gating strategy**

Describe the gating strategy used for all relevant experiments, specifying the preliminary FSC/SSC gates of the starting cell population, indicating where boundaries between "positive" and "negative" staining cell populations are defined.

- ☐ Tick this box to confirm that a figure exemplifying the gating strategy is provided in the Supplementary Information.

## Magnetic resonance imaging

### Experimental design

**Design type**

Indicate task or resting state; event-related or block design.

**Design specifications**

Specify the number of blocks, trials or experimental units per session and/or subject, and specify the length of each trial or block (if trials are blocked) and interval between trials.

**Behavioral performance measures**

State number and/or type of variables recorded (e.g. correct button press, response time) and what statistics were used to establish that the subjects were performing the task as expected (e.g. mean, range, and/or standard deviation across subjects).



## Acquisition

Imaging type(s)	<i>Specify: functional, structural, diffusion, perfusion.</i>
Field strength	<i>Specify in Tesla</i>
Sequence & imaging parameters	<i>Specify the pulse sequence type (gradient echo, spin echo, etc.), imaging type (EPI, spiral, etc.), field of view, matrix size, slice thickness, orientation and TE/TR/flip angle.</i>
Area of acquisition	<i>State whether a whole brain scan was used OR define the area of acquisition, describing how the region was determined.</i>
Diffusion MRI	<input type="checkbox"/> Used <input type="checkbox"/> Not used

## Preprocessing

Preprocessing software	<i>Provide detail on software version and revision number and on specific parameters (model/functions, brain extraction, segmentation, smoothing kernel size, etc.).</i>
Normalization	<i>If data were normalized/standardized, describe the approach(es): specify linear or non-linear and define image types used for transformation OR indicate that data were not normalized and explain rationale for lack of normalization.</i>
Normalization template	<i>Describe the template used for normalization/transformation, specifying subject space or group standardized space (e.g. original Talairach, MNI305, ICBM152) OR indicate that the data were not normalized.</i>
Noise and artifact removal	<i>Describe your procedure(s) for artifact and structured noise removal, specifying motion parameters, tissue signals and physiological signals (heart rate, respiration).</i>
Volume censoring	<i>Define your software and/or method and criteria for volume censoring, and state the extent of such censoring.</i>

## Statistical modeling & inference

Model type and settings	<i>Specify type (mass univariate, multivariate, RSA, predictive, etc.) and describe essential details of the model at the first and second levels (e.g. fixed, random or mixed effects; drift or auto-correlation).</i>
Effect(s) tested	<i>Define precise effect in terms of the task or stimulus conditions instead of psychological concepts and indicate whether ANOVA or factorial designs were used.</i>
Specify type of analysis:	<input type="checkbox"/> Whole brain <input type="checkbox"/> ROI-based <input type="checkbox"/> Both
Statistic type for inference (See <a href="#">Eklund et al. 2016</a> )	<i>Specify voxel-wise or cluster-wise and report all relevant parameters for cluster-wise methods.</i>
Correction	<i>Describe the type of correction and how it is obtained for multiple comparisons (e.g. FWE, FDR, permutation or Monte Carlo).</i>

## Models & analysis

n/a	Involved in the study
<input type="checkbox"/>	<input type="checkbox"/> Functional and/or effective connectivity
<input type="checkbox"/>	<input type="checkbox"/> Graph analysis
<input type="checkbox"/>	<input type="checkbox"/> Multivariate modeling or predictive analysis
Functional and/or effective connectivity	<i>Report the measures of dependence used and the model details (e.g. Pearson correlation, partial correlation, mutual information).</i>
Graph analysis	<i>Report the dependent variable and connectivity measure, specifying weighted graph or binarized graph, subject- or group-level, and the global and/or node summaries used (e.g. clustering coefficient, efficiency, etc.).</i>
Multivariate modeling and predictive analysis	<i>Specify independent variables, features extraction and dimension reduction, model, training and evaluation metrics.</i>